Setup and Characterization of a Single-Frequency Thin-Disk Laser Containing a Polarizing Gires-Tournois Interferometer

Marnik Metting van Rijn
marnikm@ethz.ch

Supervisors:
Manuel Zeyen
Dr. Karsten Schuhmann
Dr. Aldo Antognini
Prof. Dr. Klaus Kirch

Institute for Particle Physics and Astrophysics, ETH, 8093 Zurich, Switzerland
Laboratory for Particle Physics, Paul Scherrer Institute, 5232 Villigen-PSI, Switzerland

July 10, 2020

Abstract

We present a new frequency selective element suitable for high power laser cavities with improved heat regulation and capability of enforcing single-frequency operation. A birefringent Gires-Tournois interferometer is combined with a $\lambda/4$ plate and a linear polarizer making it a polarizing Gires-Tournois interferometer. We further present a first of its kind single-frequency thin-disk laser containing such a polarizing Gires-Tournois interferometer that acts as a wavelength selective element. The advantage lies in laser power scalability up to the kW range as thermal effects are reduced by contacting one end face of the Gires-Tournois interferometer to a heat sink. Power scalability arises from the effective cooling given the large surface to volume ratio. We used the frequency dependent polarization of the polarizing Gires-Tournois interferometer to stabilize the laser frequency with the Hänsch-Couillaud locking method. Subsequently, noise with frequency up to 2 Hz was significantly suppressed leading to single mode operation without mode hopping.

Contents

1 Introduction

1.1 Proton Radius Puzzle

Accurate values of the charge as well as the magnetization distribution inside the proton have become more important as they are considered the limiting factor when comparing experimental results and theory. In comparison to the proton radius determined by measuring the transition frequency in hydrogen and deuterium [1], the value determined using spectroscopy of the 2S-2P transition muonic hydrogen reveals a deviation of 5σ [2] and 7σ [3]. This discrepancy is known as the proton radius puzzle and remains an unsolved problem in physics since 2010.
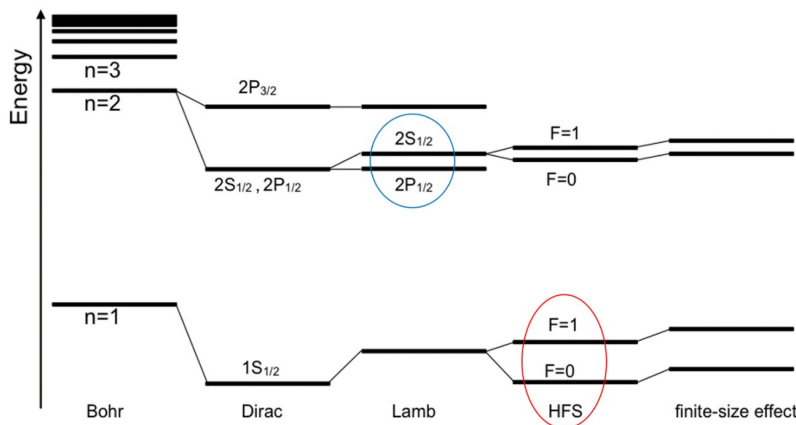
Figure 1: Energy level splitting of the hydrogen atom, where 1S-HFS is marked in red and the 2S-2P energy splitting in blue. [4]

Figure 1 shows the corrections in energy levels of the Bohr model of the hydrogen atom. The initial correction denoted as *Dirac* covers relativistic effects in the kinetic energy of the electron, spin-orbit coupling and the Darwin term which overall lead to a reduction in energy. This reduction is also known as the fine structure of the hydrogen atom. The *Lamb* shift arises due to fluctuations in the electric and magnetic field which can be derived in quantum electrodynamics. Denoted as *HFS* in Figure 1, the hyper fine splitting leads to a splitting in the energy levels. This effect covers for instance the interaction of the magnetic dipole moment of the proton with the electron. The last correction *finite-size effect* arises due the fact that the proton was initially treated as a point-like particle in the calculation of the Coulomb energy but in fact is of finite size.

This experiment pursues to determine the Zemach radius of the proton by measuring the ground-state hyperfine splitting (1S-HFS) in muonic hydrogen μp, which consists of a negative muon, μ^-, and a proton, p. The mass of the muon is about 200 times larger than the electron, which leads to a 200 times smaller Bohr radius in μp and an increased overlap between the wavefunction of the muon and the proton. This increased overlap leads to an enhancement in the finite-size effect of the proton by increasing the energy contribution by a factor of 10^7 as the finite-size effect scales by the third power [5]. Based on theoretical calculations, the HFS in muonic hydrogen contributes an energy of

$$\Delta E_{\text{HFS}} = 183.788(7) + 1.004\Delta_{\text{TPE}}, \quad [meV] \tag{1}$$

where Δ_{TPE} is the contribution of the two photon exchange [6]. If the energy ΔE_{HFS} is measured precisely, Equation (1) provides a possibility to calculate the two photon exchange energy Δ_{TPE} which splits into

$$\Delta_{\text{TPE}} = \Delta_{\text{Z}} + \Delta_{\text{recoil}} + \Delta_{\text{pol}}, \tag{2}$$

3

where Δ_{recoil} and Δ_{pol} can be calculated separately. Noting that,

$$\Delta_{\mathrm{Z}} = -2(Z\alpha)m_r R_Z, \tag{3}$$

where Z is the atomic number, α the fine structure constant and m_r the reduced mass, the Zemach radius R_Z of the proton can be determined by measuring ΔE_{HFS}.

In order to determine ΔE_{HFS} a muon beam is led into a cavity filled with H_2 gas as target, where about 25 % of the muons stop in the gas forming μp [5]. After a short time, the μp equilibrate in the $|0,0\rangle$ state which is shown in Figure 2 and where the notation $|F, m_F\rangle$ was used. A laser can then be used to induce a transition to the $|1, -1\rangle$ state provided that the frequency of the laser corresponds to the resonance frequency. A further de-excitation then results in a gain in kinetic energy of the μp which allows the μp to diffuse through the gas and reach the target walls where it can be detected. Measuring the amount of detected μp at the target walls as a function of the laser frequency results in a resonance curve from which ΔE_{HFS} can be determined.
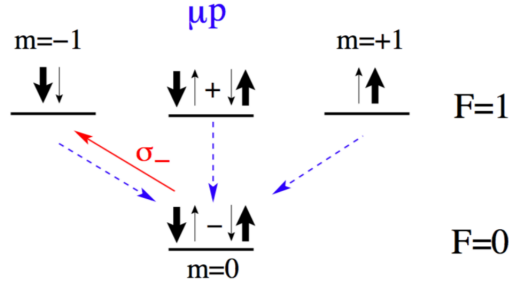
Figure 2: Detailed diagram of the HFS of muonic hydrogen, which corresponds to the red marked part in Figure 1. The arrows in blue show the spontaneous de-excitation, whereas the red arrow corresponds to a laser induced transition. [5]

1.2 Laser System and Characterization of the Seed Laser
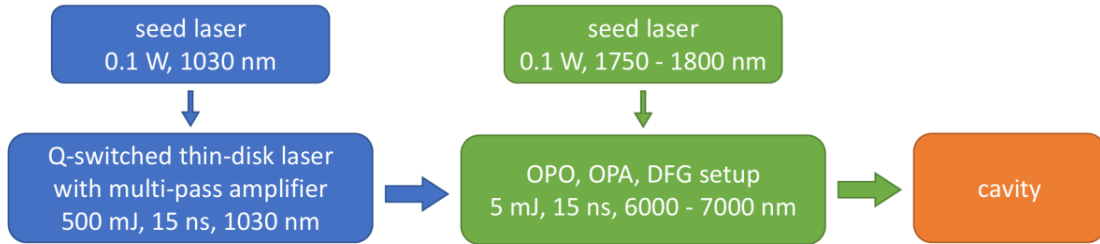
Figure 3: Schematic of the laser system. [7].

The laser system has to fulfill the following requirements in order to allow the measurement of the Zemach radius of the proton:

- At PSI, where the measurement will take place, the rate of the incoming muons is statistically distributed which therefore requires the laser to be triggered at random intervals.

- A high laser output pulse energy is needed, as the hyperfine-transition is dipole-forbidden.

- The initial laser pulse has an energy of 50 mJ at 1030 nm before being amplified to 500 mJ. Thereafter, the wavelength of the pulse is shifted to the mid-infrared region using nonlinear down-conversion stages delivering an energy of 5 mJ at 6800 nm wavelength.

- To measure the narrow atomic transition the output of the laser system has to be single-frequency, i.e., the laser bandwidth has to be < 100 MHz at 6800 nm.

Single-frequency operation is achieved by injection seeding the oscillator with a highly stable and high power CW-laser. As commercially available seed lasers at 1030 nm are very expensive and limited in output power, a new type of laser at this wavelength is described in this work. The great advantage of the presented working principle lies in the combination of the thin-disk laser technology and the intra cavity polarizing Gires-Tournois interferometer (PGTI) [8], which enables a high power output while remaining comparatively inexpensive and easy to set up.

2 Theory

2.1 Thin-Disk Lasers

A major technological advance was done by the realization of the first laser which enabled access to a plethora of applications ranging from everyday fiber-optic communication to high power laser machining in cutting-edge scientific experiments as the one presented in this work. In this Section the working principle of a laser is described where the focus lies on thin-disk lasers and their improvement over conventional rod lasers.

A premise in order to build a laser is an active medium, also known as gain medium, which can be stimulated to emit radiation. The active medium of the thin-disk laser presented in this work is made out of a ytterbium doped yttrium-aluminium-garnet, also known as Yb:YAG. Figure 4 shows the relevant energy levels to describe the emission of a photon at a wavelength of 1030 nm..
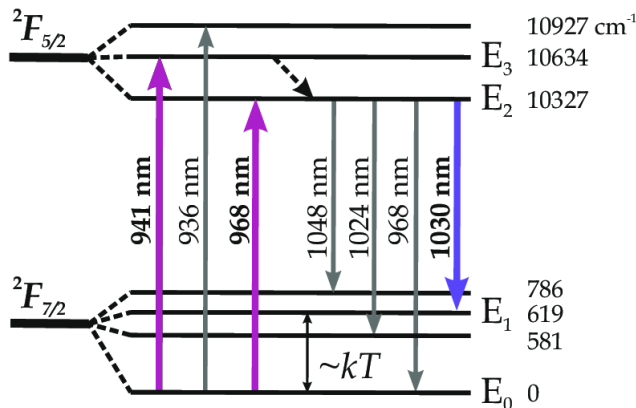
Figure 4: Diagram of the relevant energy levels in Yb:YAG, which is used as the gain medium. [9]

Starting from the ground state $\mathbf{F}_{7/2}$ E_0 the Yb^{3+} atoms are excited to the short-lived level $\mathbf{F}_{5/2}$ E_3 by a light induced energy transition. Subsequently, the atoms drop to the metastable state $\mathbf{F}_{5/2}$ E_2 where they create a population inversion with respect to the lower laser level $\mathbf{F}_{7/2}$ E_1. The de-excitation from the upper laser level to the lower laser level occurs by an emission of a photon of wavelength 1030 nm. Figure 5 shows the absorption and emission cross section of Yb:YAG, where the relevant wavelengths are denoted. As the lifetime of excited states is finite, spontaneous de-excitations occur leading to an emission of a photons.

Moreover, the emitted photons can be redirected to the active medium, where they lead to a further de-excitation of other atoms. This results in an exponential growth in number of emitted photons limited by the losses while redirecting the photons. A convenient way to capture the photons is by using two mirrors which are placed such that for every round trip the photons pass through the gain medium. The mirrors between which the photons are captured and the range between them define the laser cavity. Figure 6 shows a possible configuration of a laser cavity.

For high power laser operation however, the configuration shown in Figure 6 is not suitable as the gain medium does not allow high pump power densities without high temperature increase. Hence,
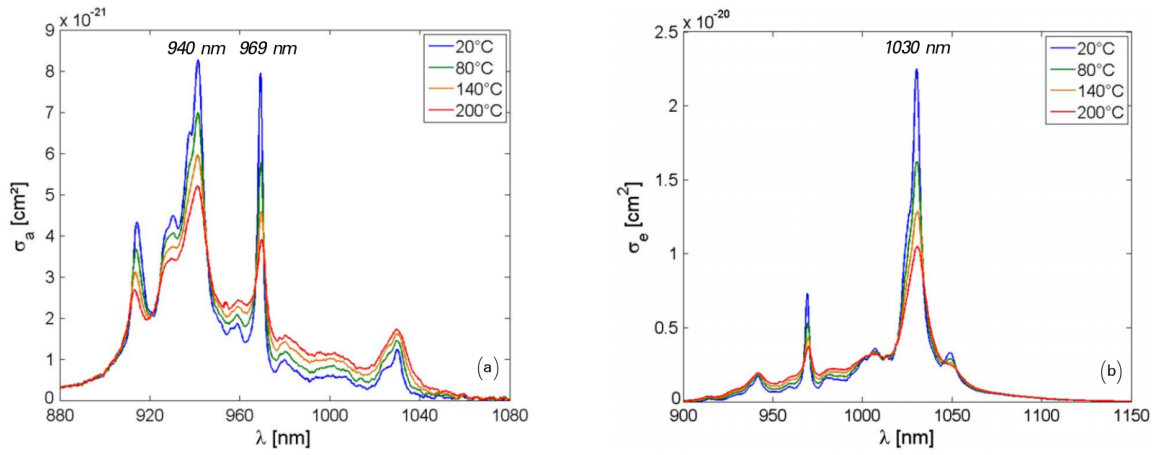
Figure 5: (a): Absorption cross section of Yb:YAG for different temperatures, where the peak absorption cross sections are marked. (b): Emission cross sections of Yb:YAG for various temperatures, where the main emission line is marked. Modified from [10].
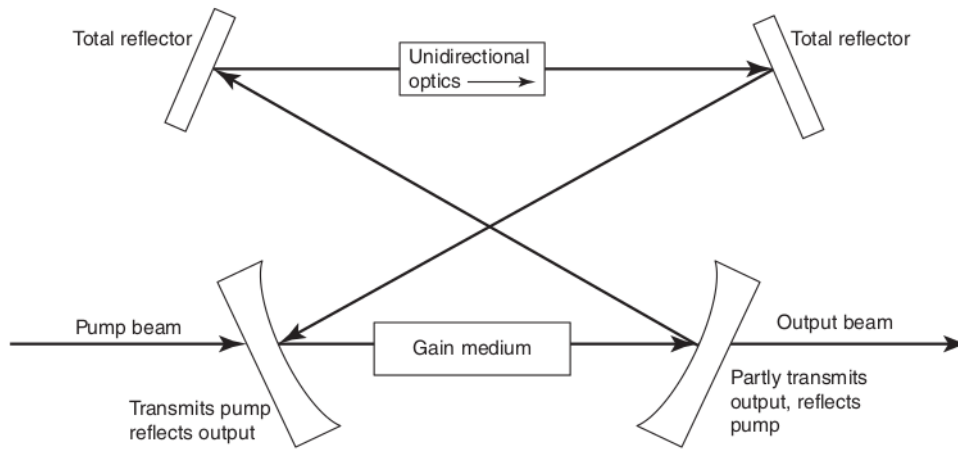
Figure 6: Example of a configuration for a laser cavity. [11]

the gain medium necessitates appropriate cooling which is limited by the surface and therefore the geometry of the gain medium. This problem was solved by the invention of thin-disk lasers [12], where the the gain medium consists of a thin-disk. An example of such a laser is shown in Figure 7. On the back side of the disk a high reflectivity coating is applied, which is why the thin-disk is also sometimes referred as an active mirror. In contrast to the geometry of the gain medium shown in Figure 6, the thin-disk has an increased surface allowing a one dimensional heat removal perpendicular to the surface. The heat dissipation can be increased by applying a heat sink at the back of the thin-disk as shown in Figure 7. Thanks to the heat flow along the laser propagation axis, the transverse temperature in the pumped region of the disk is almost constant. This highly suppresses thermal lensing effects from refractive index changes. The residual thermal lens due to the deformation of the disk is usually small but for very high power application can however become significant again. A photograph of the thin-disk of the presented laser is shown in Figure 8. Beside of other major advantages, the thin-disk laser excels conventional lasers owing to its improved power scalability [12]. The output power can be increased relatively easily by increasing the pumped area on the disk while keeping the pump power density constant. Output powers in the multi-kilowatt regime with near diffraction limited beams have been achieved from a single disk [13].

So far, the efficiency of the conversion of the power delivered by the pump light to the laser output power was not discussed in detail. In general, a laser setup draws its energy from an electrical power

6
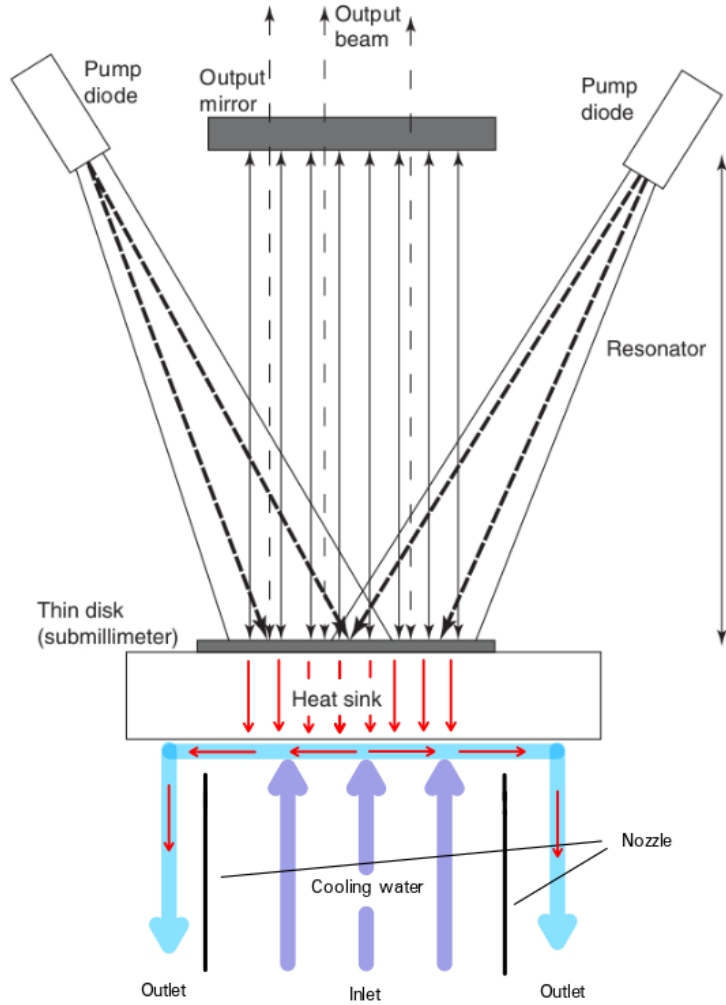
Figure 7: Laser cavity including a thin-disk, where the heat flow (red arrows) is sketched. This is realized by a continuous flow of cooling water to the back of the heat sink, which is shown for the initial, cold water (dark blue arrows) and the heat exposed flow (light blue arrows). Adapted from [11].

supply in the laboratory which leads to the natural definition of the wall-plug efficiency. In this work however, the focus lies on the characterization of the presented thin-disk laser setup which should be independent of the initial conversion from electrical power to pump light. The appropriate way to measure the efficiency is therefore given by the pump efficiency which is defined by

$$\text{pump efficiency} = \frac{\text{laser output}}{\text{pump light input}}. \tag{4}$$

2.2 Jones Formalism

The impact of optical elements on the polarization of a beam can be described by a 2x2 matrix, where the polarization is identified with a two-dimensional complex vector. This formalism is known as the Jones formalism, where the matrix is called the Jones matrix and the vector correspondingly the Jones vector. The Jones formalism facilitates calculations of laser cavities as the concatenation of several optical elements is given by matrix multiplication. Goal of this chapter is to give an overview of the Jones formalism and to derive the Jones matrix of a phase retarder which will be used to describe the single-frequency disk laser presented in this work.
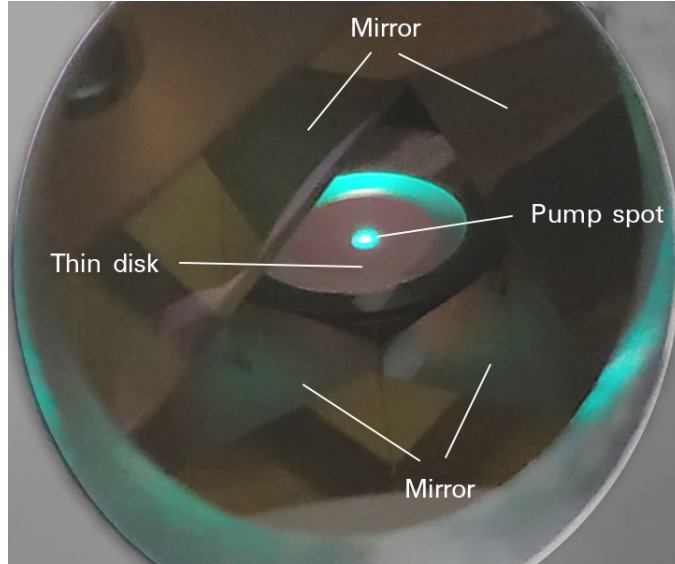
Figure 8: Photograph showing the thin-disk used in the presented laser.

In the following, all calculations and derivations are done in SI units with the convention that plane waves are expressed by $e^{i(\vec{k}\cdot\vec{x}-\omega t)}$ and the physical fields are represented by the real part.

The differential operator of the wave equation $\Box$ in media is linear and is defined as

$$\Box = \frac{1}{v^2}\frac{\partial^2}{\partial t^2} - \Delta, \tag{5}$$

where plane waves form a complete basis for all possible solutions. Taking the ansatz $\vec{E} = \vec{E_0}e^{i(\vec{k}\cdot\vec{x}-\omega t)}$ as the electric field in isotropic medium with no free charges, it follows from the first Maxwell Equation

$$\text{div}(\vec{E}) = 0 \tag{6}$$

that

$$\text{div}(\vec{E}) = \vec{E_0}\cdot\vec{\nabla}e^{i(\vec{k}\cdot\vec{x}-\omega t)} + \text{div}(\vec{E_0})e^{i(\vec{k}\cdot\vec{x}-\omega t)} = (\vec{E_0}\cdot\vec{k})ie^{i(\vec{k}\cdot\vec{x}-\omega t)}, \tag{7}$$

which has to hold at any time and for all $\vec{x}$ and therefore $\vec{E_0} \perp \vec{k}$. The magnetic field $\vec{B}$ can be obtained by noting that $(\vec{E}, \frac{c}{n}\vec{B}, \vec{k})$ forms a right-handed, orthonormal basis [14] and thus a separate discussion of the magnetic field is redundant. Since $\vec{E} \perp \vec{k}$ holds in isotropic media the two-dimensional complex plane spanned by all possible $\vec{E_0}$ can be defined as

$$\vec{k}^{\perp} = \{\vec{E_0} \in \mathbb{C}^3 | \vec{E_0} \cdot \vec{k} = 0\}, \tag{8}$$

as indicated in Figure 9. By identifying the two-dimensional real plane of the two-dimensional complex plane $\vec{k}^{\perp}$ as shown in Figure 9 an orthonormal basis $\{\hat{\vec{x}}, \hat{\vec{y}}\}$ can be found. Linear polarized light in the $\hat{\vec{x}}$-direction can be written as

$$\vec{E} = E_0 e^{i(kz-\omega t)}\hat{\vec{x}}, \tag{9}$$

where the physical field is the real part of $\vec{E}$. Same holds in $\hat{\vec{y}}$-direction

$$\vec{E} = E_0 e^{i(kz-\omega t+\phi)}\hat{\vec{y}}, \tag{10}$$

8
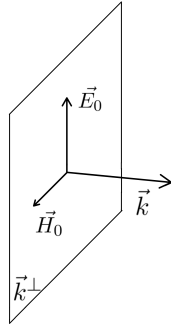
Figure 9: Sketch of a TEM mode, where $\vec{k}^{\perp}$ indicates the real part of the two-dimensional complex plane.

where a small phase difference ϕ is introduced, which can be interpreted as either a time shift (retardation) or a translation of the field in $\vec{k}$-direction. A general expression is given by the superposition of the two fields

$$\vec{E} = E_0 e^{i(kz-\omega t)}(\hat{\vec{x}} + e^{i\phi}\hat{\vec{y}}), \tag{11}$$

which in general describes an ellipse in the $\vec{k}^{\perp}$ plane for a fixed value of z, $\phi \neq 0$ and $t \in \mathbb{R}$. This is known as elliptical polarization and is the most general case. Special cases are linear polarization ($\phi \in \{0, \pi\}$), right hand circular polarization ($\phi = -\pi/2$) and left hand circular polarization ($\phi = \pi/2$) which are shown in Table 1. Equation (11) reveals that any polarization can be described by the prefactor of the basis vector $\hat{\vec{x}}$ and $\hat{\vec{y}}$. The Jones formalism or also known as Jones calculus identifies

$$E_0\hat{\vec{x}} = \begin{pmatrix} 1 \\ 0 \end{pmatrix} \qquad \text{and} \qquad E_0\hat{\vec{y}} = \begin{pmatrix} 0 \\ 1 \end{pmatrix} \tag{12}$$

which results in a shorthand notation for the polarization of the field. The vectors are called Jones vectors and are normalized to unit length[1]. A convenient way to define the basis vector is to set $\hat{\vec{x}}$ as horizontal and $\hat{\vec{y}}$ as vertical. Noting that the beam ($\vec{k}$) is usually parallel to the table on which the laser setup is mounted, horizontal would mean horizontal to the plane of the table and vertical respectively.

Linear 45°	Linear −45°	Right circular	Left circular	Elliptical
$\frac{1}{\sqrt{2}}\begin{pmatrix} 1 \\ 1 \end{pmatrix}$	$\frac{1}{\sqrt{2}}\begin{pmatrix} 1 \\ -1 \end{pmatrix}$	$\frac{1}{\sqrt{2}}\begin{pmatrix} 1 \\ -i \end{pmatrix}$	$\frac{1}{\sqrt{2}}\begin{pmatrix} 1 \\ i \end{pmatrix}$	$\frac{1}{\sqrt{2}}\begin{pmatrix} 1 \\ e^{i\pi/4} \end{pmatrix}$

Table 1: Polarization shown in the real $\vec{k}^{\perp}$ plane and the corresponding Jones vector.

The Jones formalism represents optical elements by a 2x2 matrix, where the concatenation of several optical elements is calculated by matrix multiplication. A polarizer is defined as an optical element which is opaque or transparent dependent on the polarization of the incoming beam. Examples of several polarizers and the corresponding matrices are given in Table 2.

---

[1] The norm used is the complex norm defined by $|\vec{v}| = \sqrt{\sum_{i=1}^{3} v_i v_i^*}$.

Linear horizontal	Linear vertical	Linear $\pm 45°$ to horizontal	Right circular	Left circular
$\begin{pmatrix} 1 & 0 \\ 0 & 0 \end{pmatrix}$	$\begin{pmatrix} 0 & 0 \\ 0 & 1 \end{pmatrix}$	$\frac{1}{2} \begin{pmatrix} 1 & \pm 1 \\ \pm 1 & 1 \end{pmatrix}$	$\frac{1}{2} \begin{pmatrix} 1 & i \\ -i & 1 \end{pmatrix}$	$\frac{1}{2} \begin{pmatrix} 1 & -i \\ i & 1 \end{pmatrix}$

Table 2: Polarizers and the corresponding matrices represented in the Jones formalism. The determinant of the matrices are all zero, which has the physical meaning that the listed polarizers are opaque for some particular polarizations.
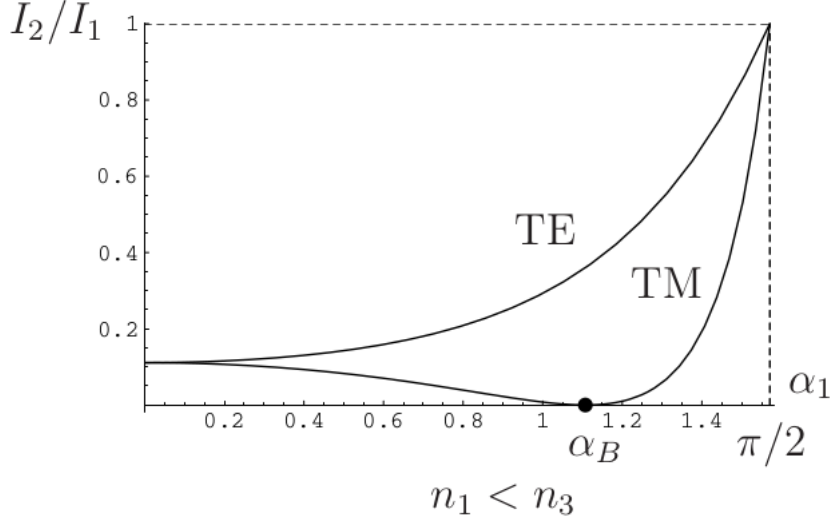
Figure 10: Intensity of the reflection I_2 as a function of the incident angle α and scaled by the intensity of the incoming beam I_1, where TE is referred to transversal electric field (s-polarized) and where TM corresponds to transversal magnetic field (p-polarized). In this notation, α_B is the Brewster's angle. [14]

A polarizer can be realized by taking a transparent plate and mounting it at Brewster's angle into the beam. This corresponds to a linear polarizer, where the orientation depends on where the Brewster's angle is situated with respect to the incident beam and the normal of the plate. Figure 10 shows the intensity of the reflected beam as a function of the incident wave, where α_B is the Brewster's angle. At this specific angle only s-polarized light is reflected, whereas the transmitted beam consists mostly out of p-polarized light. This kind of linear polarizer is realized by using thin film polarizers (TFP).

Assuming that a linear polarized beam with an angle of $-45°$ to the horizontal hits a polarizer in $+45°$ direction, no light will be transmitted since

$$\frac{1}{2} \begin{pmatrix} 1 & 1 \\ 1 & 1 \end{pmatrix} \frac{1}{\sqrt{2}} \begin{pmatrix} 1 \\ -1 \end{pmatrix} = \frac{1}{2\sqrt{2}} \begin{pmatrix} 0 \\ 0 \end{pmatrix}. \tag{13}$$

It might be the case that the polarizer is not totally opaque nor totally transparent as the following example shows, where a horizontal polarized beam hits a left circular polarizer.

$$\frac{1}{2} \begin{pmatrix} 1 & -i \\ i & 1 \end{pmatrix} \begin{pmatrix} 1 \\ 0 \end{pmatrix} = \frac{1}{2} \begin{pmatrix} 1 \\ i \end{pmatrix} \tag{14}$$

Noting that $|\frac{1}{2} \begin{pmatrix} 1 \\ i \end{pmatrix}| = \sqrt{\frac{1}{2}}$ the polarizer is not totally opaque but leads to a decrease in intensity of the beam. Another possibility to derive the result in Equation (14) is by realizing that horizontal

10

polarization can be written as a superposition of a right and left circular polarization

$$\begin{pmatrix} 1 \\ 0 \end{pmatrix} = \frac{1}{2}\left[\begin{pmatrix} 1 \\ i \end{pmatrix} + \begin{pmatrix} 1 \\ -i \end{pmatrix} \right], \tag{15}$$

where the left circular polarizer completely removes the contribution of the right circular polarization of the incoming beam.
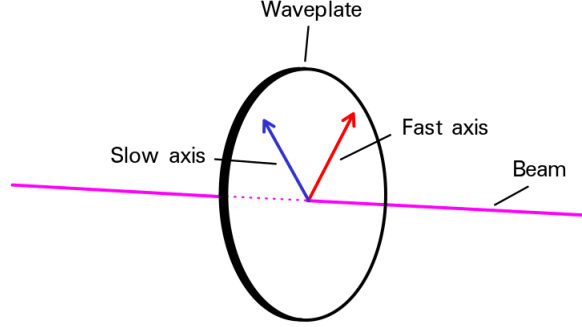
Figure 11: Fast and slow axis of a waveplate.

Apart from polarizers, there are other optical elements such as phase retarders, which are also known as waveplates. These are based on birefringent materials which have a different index of refraction for different directions in the medium and therefore induce a different phase shift for each component of the field. The direction with the lower index of refraction n_f is called the fast axis, as the phase velocity in the fast axis direction is exceeding the phase velocity in the other direction. Conversely, the direction with the higher index of refraction is called the slow axis with index of refraction n_s. Figure 11 shows a sketch of the axis in the waveplate. Placing a phase retarder with length L such that the fast axis lies in $\hat{\tilde{x}}$-direction and the slow axis in $\hat{\tilde{y}}$-direction leads to a phase change in the components by

$$\text{Fast:} \quad E_0 \mapsto E_0 e^{i(k_0 n_f L)} \tag{16}$$

$$\text{Slow:} \quad E_0 \mapsto E_0 e^{i(k_0 n_s L)}, \tag{17}$$

where k_0 is the wavevector in vacuum. By defining $\Delta n = n_s - n_f$ the Jones matrix is

$$e^{-ik_0 n_f l} \begin{pmatrix} 1 & 0 \\ 0 & e^{ik_0 \Delta n L} \end{pmatrix}, \tag{18}$$

where $e^{-ik_0 n_f l}$ can be dropped as it only gives a total phase shift. The resulting Jones matrix $\mathbf{J}$ is then given by

$$\mathbf{J} = \begin{pmatrix} 1 & 0 \\ 0 & e^{ik_0 \Delta n L} \end{pmatrix}, \tag{19}$$

where a few examples for certain values of $\Delta n L$ are shown in Table 3. If the phase retarder is rotated by an angle α around the direction of propagation, the corresponding Jones matrix $\mathbf{J}'$ is obtained by $\mathbf{J}' = \mathbf{R}_\alpha \mathbf{J} \mathbf{R}_{-\alpha}$, where the rotation matrix $\mathbf{R}_\alpha$ is defined by

$$\mathbf{R}_\alpha = \begin{pmatrix} \cos(\alpha) & -\sin(\alpha) \\ \sin(\alpha) & \cos(\alpha) \end{pmatrix}. \tag{20}$$

Quarter waveplate fast in horizontal	$\Delta n L = \lambda_0/4$	$\begin{pmatrix} 1 & 0 \\ 0 & i \end{pmatrix}$	Turns 45° linear polarized light into left circular polarized.
Quarter waveplate fast in vertical	$\Delta n L = \lambda_0/4$	$\begin{pmatrix} 1 & 0 \\ 0 & -i \end{pmatrix}$	Turns 45° linear polarized light into right circular polarized.
Half waveplate fast in horizontal	$\Delta n L = \lambda_0/2$	$\begin{pmatrix} 1 & 0 \\ 0 & -1 \end{pmatrix}$	Turns 45° polarized light into −45°. Changes the sense of circulation for circular polarized light.

Table 3: Waveplates, the corresponding Jones matrix and the effects. Only relative phase changes are shown in the Jones matrix.

2.3 Wave Propagation Matrix

Similar to the Jones matrix, the wave propagation matrix is used to calculate the effect of an optical element on the propagating wave. However, the wave propagation matrix describes the total change in phase and amplitude of the electric field induced by an optical element. In this section, the transmission curve of a Fabry-Perot interferometer is derived, which will be used to show the frequency-selective characteristic of the polarizing Gires-Tournois interferometer.
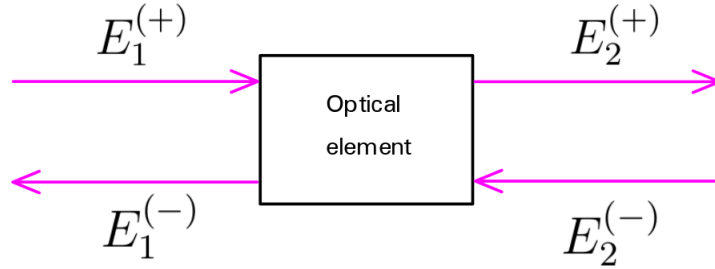
Figure 12: Sketch of the situation described in Equation (21).

As shown in Figure 12, the goal is to find a relation between the amplitude and the phase of the beam before entering the optical element (left in Figure 12) and the beam after the optical element (right in Figure 12). For example, the field $E_1^{(+)}$ of the beam reaches a phase retarder (optical element) from the left and is reflected on the surface. The reflected field is described by $E_1^{(-)}$, where the minus denotes the propagation from right to left and the subscript 1 that the field is on the left of the optical element. On the other side, the field $E_2^{(+)}$ describes the field of the outgoing beam, where the subscript 2 shows that the field has passed the phase retarder and the plus indicates the direction going from left to right. Subsequently, $E_2^{(-)}$ is zero, as no light is coming from the right in this example. This can mathematically be treated by introducing the wave propagation matrix $\mathbf{W}$. The general expression is

$$\begin{pmatrix} E_2^{(+)} \\ E_2^{(-)} \end{pmatrix} = \begin{pmatrix} A_{12} & B_{12} \\ C_{12} & D_{12} \end{pmatrix} \begin{pmatrix} E_1^{(+)} \\ E_1^{(-)} \end{pmatrix}, \tag{21}$$

where $E_1^{(+)}$ and $E_1^{(-)}$ are by convention either s-polarized or p-polarized components of the beam. Similar to the Jones formalism, the concatenation of optical elements is mathematically treated by matrix multiplication, where the subscript is increased by 1 after passing one optical element. For example, the propagation of the distance l in a uniform medium with index of refraction n is represented by the matrix

$$\begin{pmatrix} A & B \\ C & D \end{pmatrix} = \begin{pmatrix} e^{-iknl} & 0 \\ 0 & e^{iknl} \end{pmatrix}. \tag{22}$$

Similar to the wave propagation matrix introduced in Equation (21), the scattering matrix $\mathbf{S}$ relates the incoming fields $E_1^{(+)}$ and $E_2^{(-)}$ with the scattered fields $E_2^{(+)}$ and $E_1^{(-)}$ by

$$\begin{pmatrix} E_2^{(+)} \\ E_1^{(-)} \end{pmatrix} = \begin{pmatrix} a_{12} & b_{12} \\ c_{12} & d_{12} \end{pmatrix} \begin{pmatrix} E_1^{(+)} \\ E_2^{(-)} \end{pmatrix}. \tag{23}$$

The wave propagation can be converted into a scattering matrix by

$$\begin{pmatrix} a & b \\ c & d \end{pmatrix} = \frac{1}{D} \begin{pmatrix} AD - BC & B \\ -C & 1 \end{pmatrix} \tag{24}$$

and symmetrically

$$\begin{pmatrix} A & B \\ C & D \end{pmatrix} = \frac{1}{d} \begin{pmatrix} ad - bc & b \\ -c & 1 \end{pmatrix}. \tag{25}$$

An illustration of the advantage of the scattering matrix can be shown by means of an example of an interface between two media. In that case the scattering matrix is given by

$$\mathbf{S} = \begin{pmatrix} t_{12} & r_{21} \\ r_{12} & t_{21} \end{pmatrix}, \tag{26}$$

where t and r are the complex amplitude coefficients. This relation is important as it is more convenient to use the scattering matrix when the transmission coefficient T and reflection coefficient R are of interest. The coefficients are related to the complex amplitude coefficients by

$$R = |r|^2 \quad \text{and} \quad T = 1 - R. \tag{27}$$
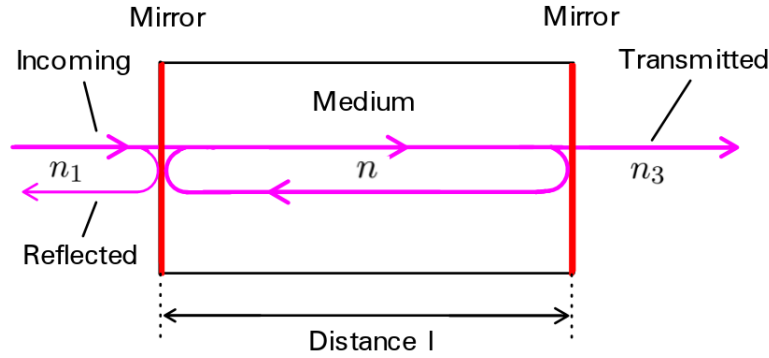
Figure 13: Schematic of an FPI.

A Fabry-Perot interferometer (FPI) is an optical resonator consisting of two mirrors placed parallel to each other. Due to the reflectivity of the mirrors, a beam entering the resonator will interfere with itself resulting in an amplification for the resonant frequencies and destructive interference for off-resonant frequencies. The wave propagation matrices for the two mirrors separately are given by

$$\frac{1}{(1 - r_{12})} \begin{pmatrix} 1 & -r_{12} \\ -r_{12} & 1 \end{pmatrix} \quad \text{and} \quad \frac{1}{(1 - r_{23})} \begin{pmatrix} 1 & -r_{23} \\ -r_{23} & 1 \end{pmatrix}. \tag{28}$$

For the propagation of length l in media, the matrix in Equation (22) can be used. Since an FPI consists of two mirrors separated by the distance l, these three matrices can be multiplied to find the total wave propagation matrix

13

$$\mathbf{W} = \begin{pmatrix} \dfrac{e^{-ikln}\left(1 + e^{2ikln}r_{12}r_{23}\right)}{(-1+r_{12})(-1+r_{23})} & -\dfrac{e^{-ikln}\left(r_{12} + e^{2ikln}r_{23}\right)}{(-1+r_{12})(-1+r_{23})} \\ -\dfrac{e^{-ikln}\left(e^{2ikln}r_{12} + r_{23}\right)}{(-1+r_{12})(-1+r_{23})} & \dfrac{e^{-ikln}\left(e^{2ikln} + r_{12}r_{23}\right)}{(-1+r_{12})(-1+r_{23})} \end{pmatrix} \tag{29}$$

and the related scattering matrix

$$\mathbf{S} = \begin{pmatrix} \dfrac{e^{ikln}(1+r_{12})(1+r_{23})}{e^{2ikln} + r_{12}r_{23}} & -\dfrac{r_{12} + e^{2ikln}r_{23}}{e^{2ikln} + r_{12}r_{23}} \\ \dfrac{e^{2ikln}r_{12} + r_{23}}{e^{2ikln} + r_{12}r_{23}} & \dfrac{e^{ikln}(-1+r_{12})(-1+r_{23})}{e^{2ikln} + r_{12}r_{23}} \end{pmatrix}. \tag{30}$$

If an FPI is surrounded by air, the index of refraction n_1 and n_3 are equal and close to unity which implies that $r_{12} = r_{32}$. Further, the relation $r_{12} = -r_{21}$ and $t_{12} = 1 + r_{12}$ hold which yield the wave propagation matrix for an FPI

$$\mathbf{W_{FPI}} = \frac{1}{4n} \begin{pmatrix} (1+n)^2 e^{-iknl} - (1-n)^2 e^{iknl} & -2i(n^2-1)\mathrm{sin}knl \\ 2i(n^2-1)\mathrm{sin}knl & (1+n)^2 e^{iknl} - (1-n)^2 e^{-iknl} \end{pmatrix}, \tag{31}$$

where the Fresnel equations were used in the case of normal incidence. This can be rewritten as a scattering matrix using the relation given in Equation (25). Hence, the transmitted intensity can be calculated using the scattering matrix which yields [15]

$$I_4^+ = \frac{1}{1 + (2\mathcal{F}/\pi)^2\mathrm{sin}^2(knl)} I_1^+, \tag{32}$$

where the finesse

$$\mathcal{F} = \frac{\pi\sqrt{R}}{1-R} \tag{33}$$

was introduced and the definition of $R = |r_{12}|^2$ was used.

Figure 14 shows that the transmission of the FPI peaks at each resonance frequency. The distance between the resonances are given by

$$\Delta f_{\mathrm{FPI}} = \frac{c}{2nl}, \tag{34}$$

which is known as the free spectral range (FSR) of the FPI. An alternative definition of the finesse is obtained by taking the quotient of the FSR and the bandwidth of each resonance as

$$\mathcal{F} = \frac{\Delta f_{\mathrm{FPI}}}{\delta f_{\mathrm{FPI}}}, \tag{35}$$

where δf_{FPI} is the full width at half-maximum of the peak.

An application of an FPI is as reference cavity which can be used to determine the frequency spectrum of a laser beam. In order to reach high resolution i.e. large values of $\mathcal{F}$, the mirrors of the reference cavities often have very high reflectivity ($> 97\%$). The reference cavity used to determine the spectrum of the laser presented in this work has a piezoelectric element which enables an adjustable distance between the two mirrors. The frequency spectrum of the laser can therefore be found by measuring the intensity transmitted through the reference cavity as a function of the mirror's distance. Furthermore, the two mirrors of the reference cavity are mounted in a cylinder made out of Invar, which has a very low coefficient of thermal expansion and therefore minimizing the impact of temperature variations. This is important, as a temperature drift leads to an uncertainty whether the frequency of the laser was drifting or the distance of the mirrors in the reference cavity has changed.
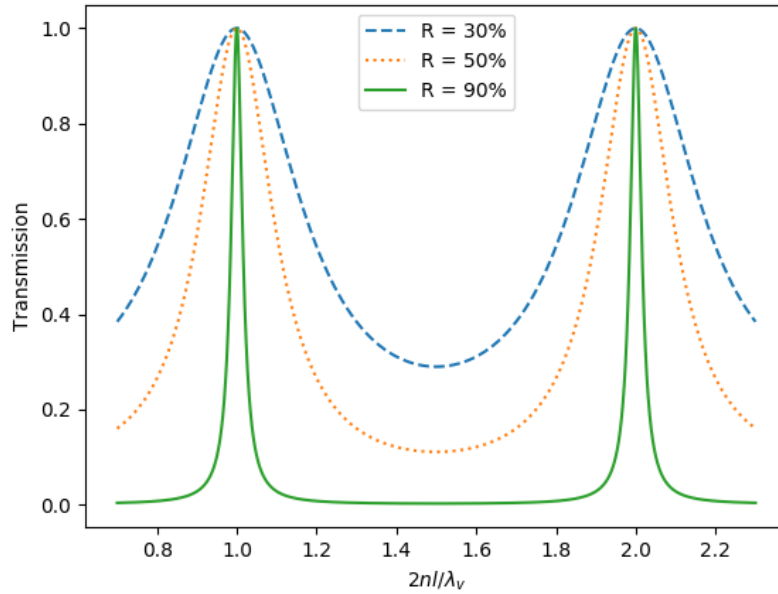
Figure 14: Transmission curve of an FPI given by Equation (32) for different reflectivity and $I_1^{(+)} = 1$. In the x-axis label λ_v corresponds to the wavelength in vacuum.
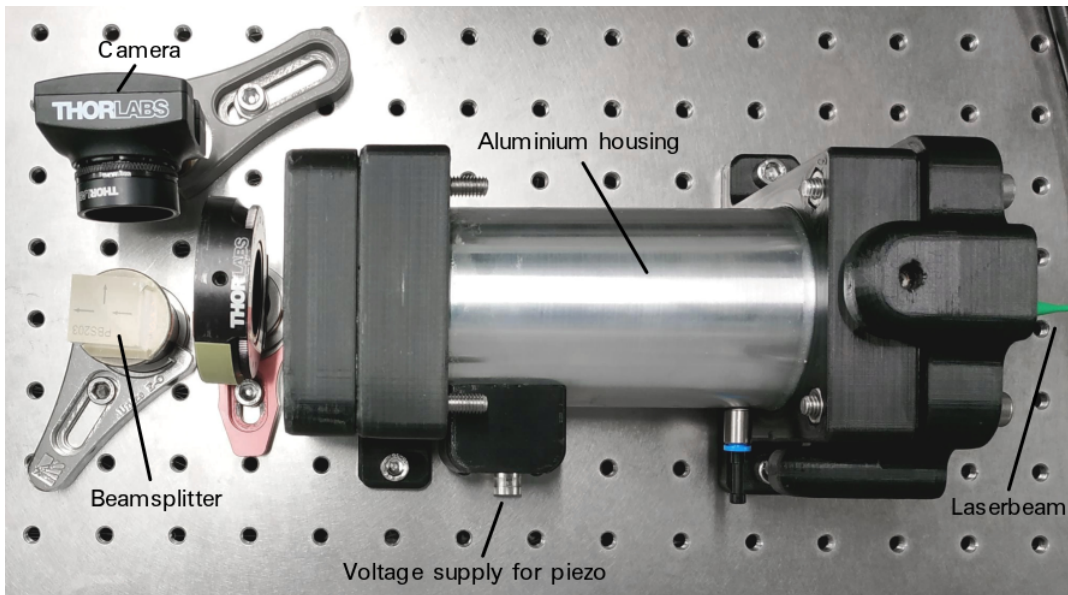
Figure 15: Reference cavity used to determine the spectrum of the laser.

An illustration of the reference cavity used to take the measurements in Section 4.2 is shown in Figure 15.

Another application of the FPI is as a frequency-selective element inside a laser cavity, since a substantial part of the frequencies are attenuated as shown in Figure 14. In this case the concept of the FPI is pushed quite far, as the FPI is no longer consisting of two mirrors, but a thin piece of e.g. fused silica. In this case one talks of an etalon. Even for low surface-reflectivity ($< 4\%$) a frequency selection can be achieved, as the attenuated frequencies fall beneath the loss-threshold of the laser. Moreover, adding several etalons in the laser cavity can result in single longitudinal mode operation. However, an etalon potentially heats up in high power laser cavities, which leads to a

non-homogeneous change in index of refraction as well as a deformation of the etalon. This follows from the intensity distribution in transverse direction of the beam which is having typically a Gaussian profile (see Figure 16). Overall, this effect can lead to a misalignment of the laser and consequently result in a loss in beam quality. As shown in the following Section, this problem can be solved by using a polarizing Gires-Tournois interferometer in the cavity, which is a frequency-selective element capable of sustaining high power beams.

Figure 16: Intensity in the transverse direction of a Gaussian beam. [11]

2.4 Polarizing Gires-Tournois Interferometer

In contrast to the FPI, the mirrors of the Gires-Tournois interferometer (GTI) have different reflectivity, where one of them is partially reflective (PR) while the other is highly reflective (HR). Ideally, the HR mirror has a reflectivity close to unity with transmission coefficient $t_{23} = 0$.
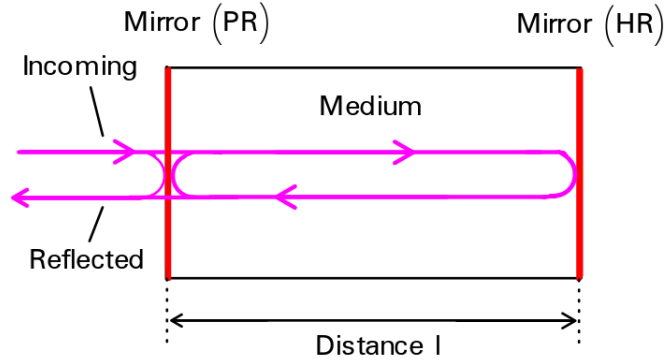
Figure 17: Schematic of a GTI.

Therefore, the reflection coefficient r_{23} is -1, which can be plugged into the scattering matrix in Equation (30). For the GTI, the important coefficient relates the incoming field $E_1^{(+)}$ to the reflected field $E_1^{(-)}$ which is the c entry (see Equation (23)) of the scattering matrix given by

$$\frac{e^{2ikln}r_{12} + r_{23}}{e^{2ikln} + r_{12}r_{23}} = \frac{\sqrt{R} - e^{-2ikln}}{1 - \sqrt{R}e^{-2ikln}}, \tag{36}$$

where the reflectivity (PR) was defined as $\sqrt{R} = r_{12}$ and thus

$$E_1^{(-)} = \frac{\sqrt{R} - e^{-2ikln}}{1 - \sqrt{R}e^{-2ikln}}E_1^{(+)}. \tag{37}$$

Provided that the HR mirror has reflectivity close to unity, an incoming wave only gains a change in phase but no change in amplitude. This motivates the ansatz $E_1^{(-)} = e^{i\phi}E_1^{(+)}$ which leads to a phase

change ϕ

$$\phi = \arctan\left[\frac{\sin(2ikln)(1-R)}{2\sqrt{R} - \cos(2ikln)(1+R)}\right]. \tag{38}$$
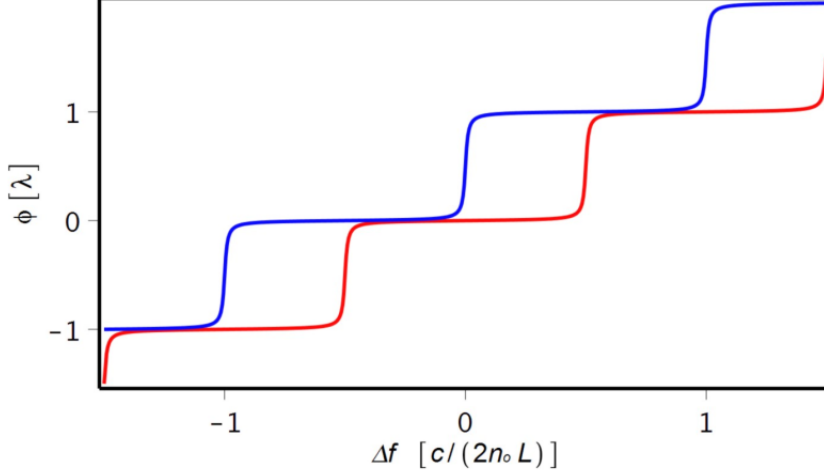
Figure 18: Induced phase difference ϕ as a function of the frequency for two different indices of refraction $n_e = 1.5433$ (red) and $n_0 = 1.5346$ (blue). This simulation corresponds to a wavelength $\lambda = 1030$ nm and a thickness $l = 147$ μm. [8]

Similar to the FPI, the resonance frequency of a GTI is defined as

$$\Delta f_{\text{res}} = \frac{c}{2ln}. \tag{39}$$

As shown in Figure 18 (blue curve), crossing the resonance frequency results in a change in phase by 2π. Away from the resonance frequency however, the occurring phase remains approximately constant before reaching the adjacent multiple of the resonance frequency. In contrast to the blue curve, the resonance frequency of the red curve is shifted by half of a free spectral range which arises from the different index of refraction. Physically this can be realized in a GTI by using a birefringent material between the two mirrors. Noting that the electric field of a beam is perpendicular to the direction of propagation (see Equation (7)), only the transverse indices of refraction of the birefringent material have an effect. Defining n_o the ordinary and n_e the extraordinary index of refraction, the Jones matrix of the birefringent Gires-Tournois interferometer (BGTI) is

$$\mathbf{J}_{\text{BGTI}} = \begin{pmatrix} \dfrac{\sqrt{R} - e^{-2ikln_o}}{1 - \sqrt{R}e^{-2ikln_o}} & 0 \\ 0 & \dfrac{\sqrt{R} - e^{-2ikln_e}}{1 - \sqrt{R}e^{-2ikln_e}} \end{pmatrix}, \tag{40}$$

where n_o is the index of refraction in $\begin{pmatrix} 1 \\ 0 \end{pmatrix}$ direction and n_e is the index of refraction in $\begin{pmatrix} 0 \\ 1 \end{pmatrix}$ direction. The general expression for the difference in relative phase delay induced by the different indices of refraction in the BGTI is given by [8]

$$\Delta\phi = \phi_e - \phi_o = 2\arctan\left(\frac{1-R}{2\sqrt{R} \cdot \sin(4\pi il\bar{n}fc^{-1})}\right), \tag{41}$$

where $\bar{n} = (n_e + n_o)/2$ was defined. This equation holds under the assumption that the substrate parameters were chosen in such a way that one pass through the material causes a phase delay of $\lambda/4$, which is fulfilled if $(n_e - n_o)l = (k \pm 1/4)\lambda$ holds.

17
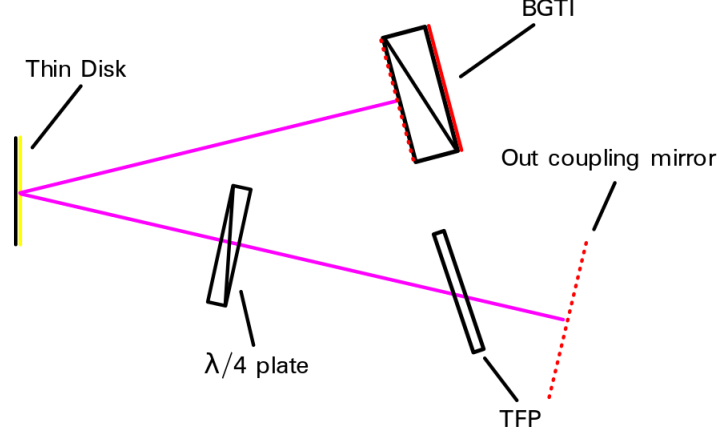
Figure 19: Example of a setup including a PGTI in a thin-disk laser cavity.

Simply mounting a BGTI in a laser cavity does not lead to a frequency selection. However, a frequency-selective element can be built by combining a TFP (horizontal transmission), a $\lambda/4$ plate and the BGTI [8]. The axis of the $\lambda/4$ plate and the BGTI are rotated by 45° with respect to the horizontal. In the following the effects of the concatenation

$$\text{TFP} \quad \circ \quad R_{-45°} \quad \circ \quad \lambda/4 \quad \circ \quad \text{BGTI} \quad \circ \quad \lambda/4 \quad \circ \quad R_{45°} \quad \circ \quad \text{TFP}$$

is studied by the means of critical examples before elaborating the mathematical aspects. A schematic of this concatenation of optical elements is shown in Figure 19, where this combination is called a polarizing birefringent Gires-Tournois interferometer (PGTI).

Table 4 shows the effects of the PGTI on a given polarization coming from the out-coupling mirror. The main result is that under ideal conditions the PGTI is frequency-selective while transmitting only p-polarized light on resonant frequencies. This can be mathematically treated by Jones matrices, which were introduced in Section 2.2. The Jones matrix for the PGTI is given by

$$\mathbf{J}_{\text{PGTI}} = \frac{1}{2} \begin{pmatrix} 1 & 0 \\ 0 & 0 \end{pmatrix} \begin{pmatrix} 1 & 1 \\ -1 & 1 \end{pmatrix} \begin{pmatrix} 1 & 0 \\ 0 & -i \end{pmatrix} \begin{pmatrix} \frac{\sqrt{R}-e^{-2ikln_o}}{1-\sqrt{R}e^{-2ikln_o}} & 0 \\ 0 & \frac{\sqrt{R}-e^{-2ikln_e}}{1-\sqrt{R}e^{-2ikln_e}} \end{pmatrix} \begin{pmatrix} 1 & 0 \\ 0 & -i \end{pmatrix} \begin{pmatrix} 1 & -1 \\ 1 & 1 \end{pmatrix} \begin{pmatrix} 1 & 0 \\ 0 & 0 \end{pmatrix}$$

which equates to

$$\mathbf{J}_{\text{PGTI}} = \begin{pmatrix} \frac{\sqrt{R}-e^{-2ikln_o}}{1-\sqrt{R}e^{-2ikln_o}} - \frac{\sqrt{R}-e^{-2ikln_e}}{1-\sqrt{R}e^{-2ikln_e}} & 0 \\ 0 & 0 \end{pmatrix}. \tag{42}$$

Under ideal conditions the beam propagating between the out coupling mirror and the rotation is purely p-polarized light which is described by the Jones vector $\begin{pmatrix} 1 \\ 0 \end{pmatrix}$. Therefore, the relation between the beam entering the PGTI E_i and the propagated beam through the PGTI E_f

$$\begin{pmatrix} E_f \\ 0 \end{pmatrix} = \mathbf{J}_{\text{PGTI}} \begin{pmatrix} E_i \\ 0 \end{pmatrix} \tag{43}$$

can be described by

$$T(k) = \left(\frac{E_f}{E_i} \right)^2 \tag{44}$$

18

Polarization	s-pol	p-pol	linear $\frac{1}{\sqrt{1+\gamma^2}}\begin{pmatrix}1\\\gamma\end{pmatrix}$	circular $\frac{1}{\sqrt{1+\gamma^2}}\begin{pmatrix}1\\\gamma i\end{pmatrix}$
TFP	0	p-polarized	p-polarized	p-pol
$R_{-45°}$	0	45° linear	45° linear	45° linear
$\lambda/4$	0	r-circular	r-circular	r-circular
BGTI	0	l-circular	l-circular	l-circular
$\lambda/4$	0	45° linear	45° linear	45° linear
$R_{45°}$	0	p-polarized	p-polarized	p-polarized
TFP	0	p-polarized	p-polarized	p-polarized
Intensity	0	1	$\frac{1}{\sqrt{1+\gamma^2}}$	$\frac{1}{\sqrt{1+\gamma^2}}$

(a) On resonance

Polarization	s-pol	p-pol	linear $\frac{1}{\sqrt{1+\gamma^2}}\begin{pmatrix}1\\\gamma\end{pmatrix}$	circular $\frac{1}{\sqrt{1+\gamma^2}}\begin{pmatrix}1\\\gamma i\end{pmatrix}$
TFP	0	p-polarized	p-polarized	p-pol
$R_{-45°}$	0	45° linear	45° linear	45° linear
$\lambda/4$	0	r-circular	r-circular	r-circular
BGTI	0	r-circular	r-circular	r-circular
$\lambda/4$	0	−45° linear	−45° linear	−45° linear
$R_{45°}$	0	s-polarized	s-polarized	s-polarized
TFP	0	0	0	0
Intensity	0	0	0	0

(b) Off resonance.

Table 4: Different initial polarizations propagated under ideal conditions through each element in order to illustrate the corresponding effect. At resonance the BGTI induces a relative phase shift of π which is equal to a $\lambda/2$ plate, whereas off resonance the BGTI induces no relative phase shift. The resulting intensity is only valid for an ideal linear polarizer.

where T is a scalar. Calculating the Jones matrix for the PGTI and taking the first entry yields [8]

$$T(f) = \frac{(R-1)^2}{(R+1)^2 - 4R\cos^2(4\pi i L \bar{n} f c^{-1})}. \tag{45}$$
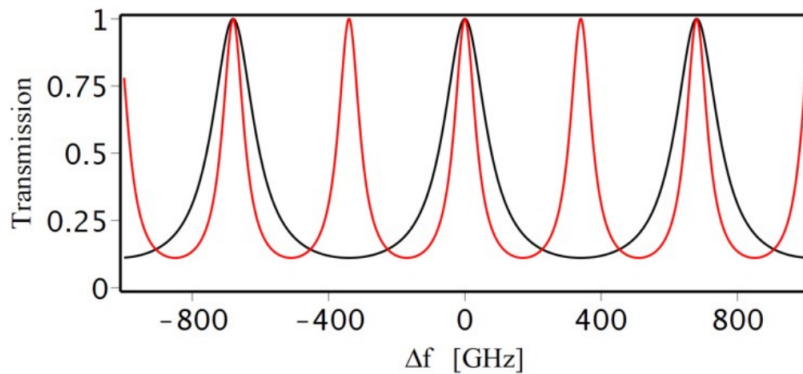
Figure 20: The transmission T of the PGTI (red) as a function of the frequency as given in Equation (45), whereas the black curve corresponds to an FPI with same thickness $L = 147$ μm and same reflectivity of $R = 50\%$. [8]

A plot of Equation (45) is shown in Figure 20 which includes a comparison to a regular FPI with

identical reflectivity R and thickness L. In comparison to the FSR of an FPI (Equation (34)), the FSR of the PGTI

$$\Delta f_{\mathrm{PGTI}} = \frac{c}{4\bar{n}L} \tag{46}$$

differs by a factor of 2. Generally, FPIs with a reflectivity of 50% are rarely used in high power laser cavities as the heat absorption increases with increasing reflectivity. However, the advantage of high reflectivity in the FPI lies in the finesse $\mathcal{F}$ defined in Equation (33) as a higher value in finesse leads to better frequency selection. Similar to the transformation from rod lasers to thin-disk lasers, the BGTI can be seen as an improvement over the FPI concerning heat management. By applying a heat sink at the back of the HR mirror efficient cooling can be done over the whole surface. In order to keep track of the temperature of the BGTI, a temperature sensor is inserted in the center of the heat sink. By mounting a Peltier element to the heat sink, the temperature of the BGTI can further be controlled by varying the applied current on the Peltier element. Drifting in resonance frequency which occurs due to the change in index of refraction arising from the applied high power laser can therefore be prevented. It shall be noted that this frequency-selective element arises from a similar approach as presented in [16].

In conclusion, the PGTI enables frequency selection with a finesse similar to an FPI with a reflectivity of 50% or higher, which is not suitable for high power laser cavities.

2.5 Hänsch-Couillaud Locking

In contrast to Section 2.4 where the TFP was assumed to be ideal, this Section relies on the fact that the TFP is not totally opaque for s-polarized light. A change in frequency will therefore induce a change in polarization of the laser beam which can be measured. This measured signal can be used to give a feedback to the length of the laser cavity and therefore increasing the stabilization of the laser frequency.
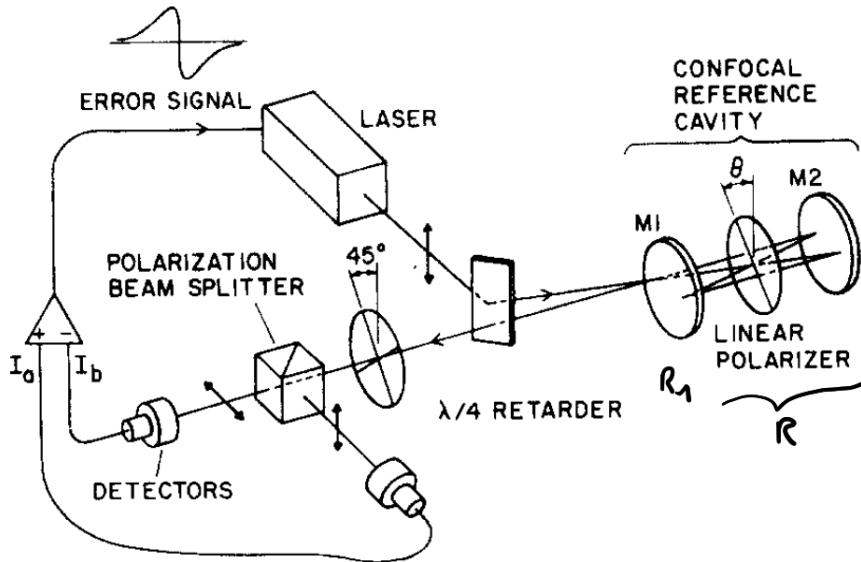
Figure 21: Example of a laser setup with Hänsch-Couillaud locking. Adapted from [17].

The cavity and the components of a laser are exposed to several perturbations which may lead to a decrease in stability of the laser frequency. As a precise and stable frequency is essential for this experiment, the frequency of the laser has to be locked, which is defined as the procedure to fix the output frequency to a reference value. As an example, the setup shown in Figure 21 is studied. The measured difference in intensities at the photodiodes I_a and I_b is given by [17]

$$I_a - I_b = I^{(i)} 2\cos\theta\sin\theta \frac{T_1 R\sin\delta}{(1-R)^2 4R\sin^2\frac{1}{2}\delta}, \tag{47}$$

where δ is the picked up phase, $I^{(i)}$ the initial intensity and R, θ and R_1 defined as shown in Figure 21. The procedure leading to this error signal is known as Hänsch-Couillaud locking.
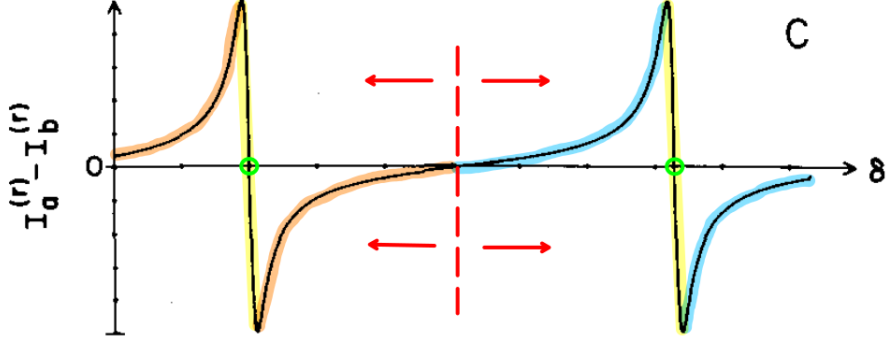
Figure 22: Plot of Equation (47). The red line divides the frequency range into two subparts (orange and blue) corresponding to the locking point (green circle). The yellow part denotes a range where the error signal is a steep, linear response. Adapted from [17].

Figure 22 shows the error signal which is used as a feedback to the laser. The locking point is circled in green. In the vicinity of the locking point, the error signal leads to a readjustment back to the locking point, which is however bounded by the line marked in red. If the frequency is changed dramatically to such a degree that it crosses the red line, the error signal pushes the frequency to the adjacent locking point. In comparison to other locking mechanisms, the Hänsch-Couillaud locking is able to absorb larger accidental frequency jumps [17], as the orange and respectively the blue sections have an increased span at which the error signal is non-zero. Therefore, re-locking to the locked frequency is possible. A great advantage of the Hänsch-Couillaud locking lies in the yellow section, where the error signal is linear. In this section the response to a possible frequency shift is very sensitive which arises from the steep gradient. In summary, the Hänsch-Couillaud locking provides a frequency locking with a large range of impact and a very sensitive linear range.

Provided that the BGTI is on resonance, the resulting beam exiting the laser cavity is almost completely p-polarized. Here, theory and practice diverge due to the fact that the TFP is not absolute opaque for s-polarized light. This however can be used to analyze the frequency, as the polarization in the PGTI changes as a function of the frequency (see Figure 18). A change in frequency would therefore lead to a different angle in linear polarization and the relationship between this angle and the resonance frequency is close to linear. It thereby fulfills the requirements for the Hänsch-Couillaud locking. As shown in Figure 23 the exiting beam is then split into two linear polarization components and analyzed. Further, this error signal is used as a feedback to the laser. The feedback signal is applied on the piezo of the out coupling mirror and therefore changing the length of the cavity. Ideally, the impact of the perturbations on the laser cavity and its component is limited in such a way, that the frequency does not leave the linear range.
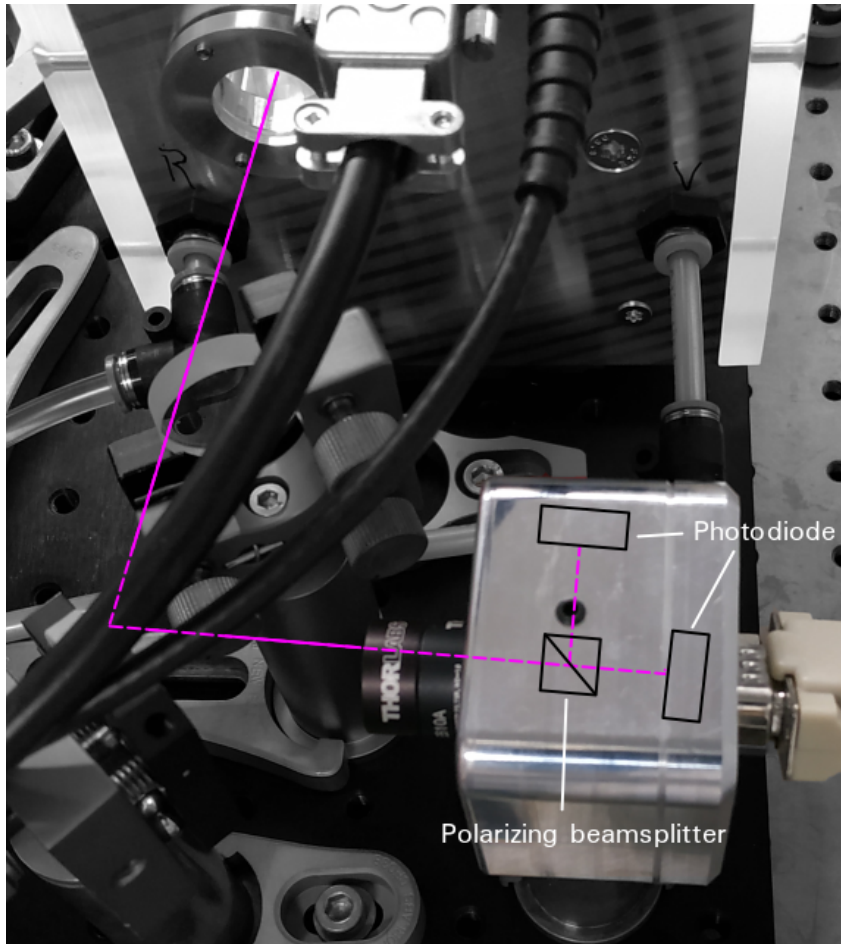
Figure 23: Setup of the components used for the creation of the error signal of the Hänsch-Couillaud locking in this experiment, where the sketched parts are inside the housing.

3 Setup and Procedures to Increase Stabilization

3.1 Schematic of the Laser

In this Section the PGTI is upgraded to a fully functional single-frequency laser. The schematic describing this extension and the realization are presented while providing details of the previously discussed optical elements.

Figure 24 shows the schematic of the laser from vertical aerial view. Starting from the thin-disk, the pump light is guided to the thin-disk by a parabolic mirror, which enables several passes over the disk. In addition to the PGTI, an etalon with low reflectivity is mounted to the beam line for further frequency selection. By applying a Peltier element[2] at the backside of the BGTI, the temperature of the birefringent material can be adjusted leading to a different index of refraction. This allows a direct intervention in the optical path length of the cavity and enables a possibility for stabilization procedures. Similar to the Peltier element, a piezoelectric element[3] (piezo) also allows a change of the length of the cavity by applying different voltage on it. In this work, the piezo will be driven by the feedback signal from the Hänsch-Couillaud leading to a more stable frequency. The realization of the laser described in the schematic is shown in Figure 25. In addition, the water-cooling system and the mechanical parts are visible from a vertical point of view.

---

[2]More information can be found in [18].

[3]A profound derivation of the piezoelectric effect and its properties are shown in [19].
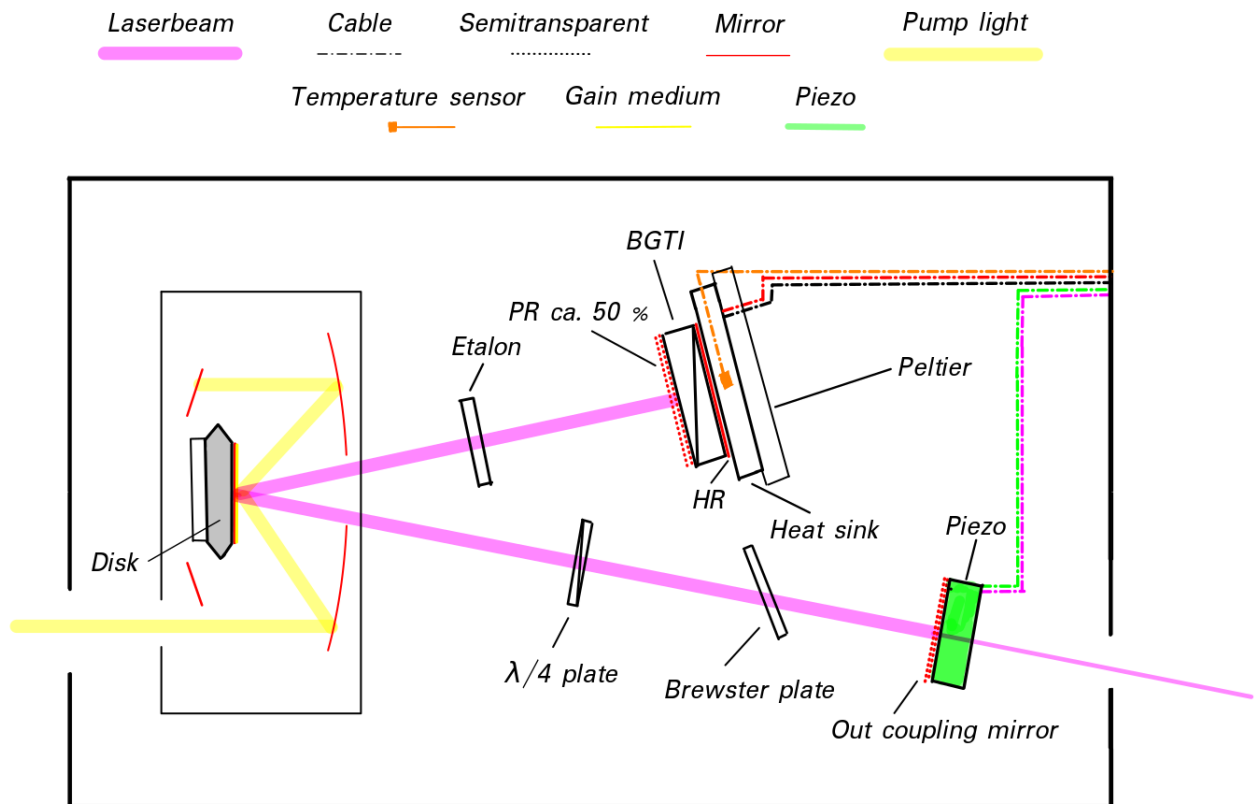
Figure 24: Schematic of the V-shaped laser cavity.
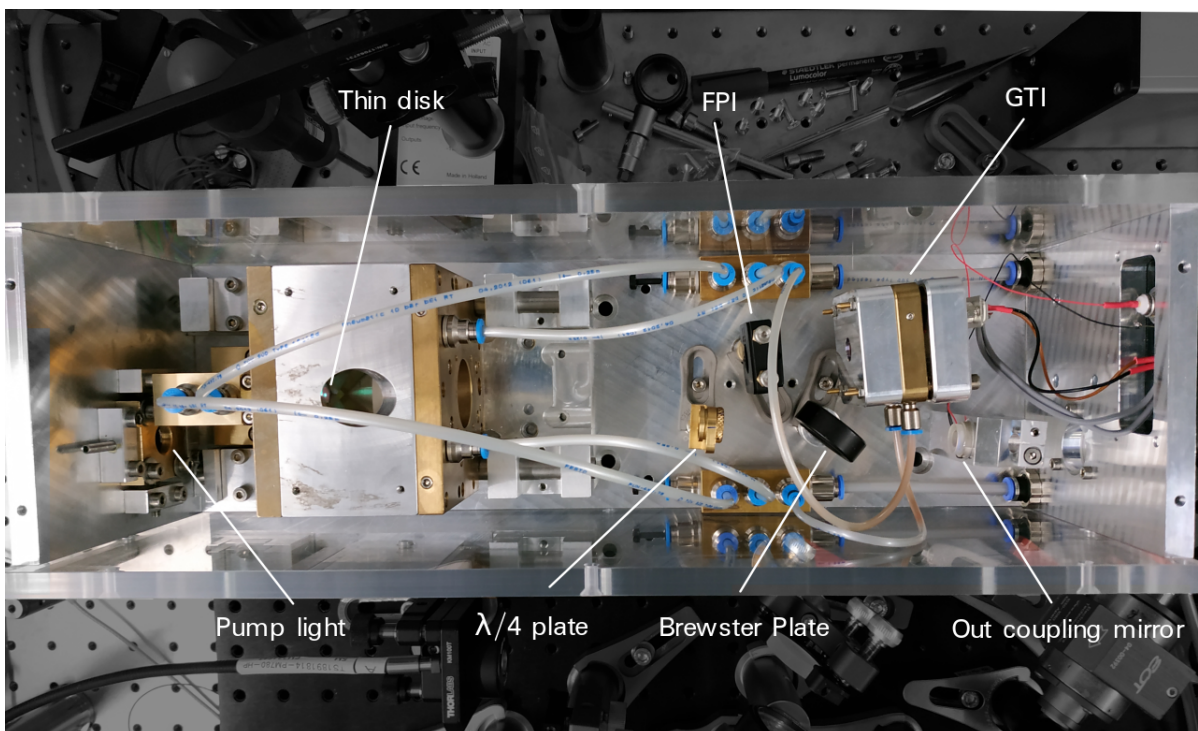
Figure 25: Vertical aerial photograph of the laser setup.

3.2 Setup: Container and Platform

In order to minimize perturbations on the frequency of the laser, several mechanical measures are presented to increase the stability.

A substantial part from the perturbations arise from vibrations which can be suppressed mechanically. As a first measure, the separate plate on which the laser container is situated is elevated using four rubber feet. On top of this plate, a 2 cm rubber sheet is placed to further minimize vibrations. Finally, the container of the laser is set on top of the rubber layer creating an important isolation from vibrations arising from the ground. In order to decrease the effect of an airflow, the container is entirely closed from the environment as shown in Figure 26.
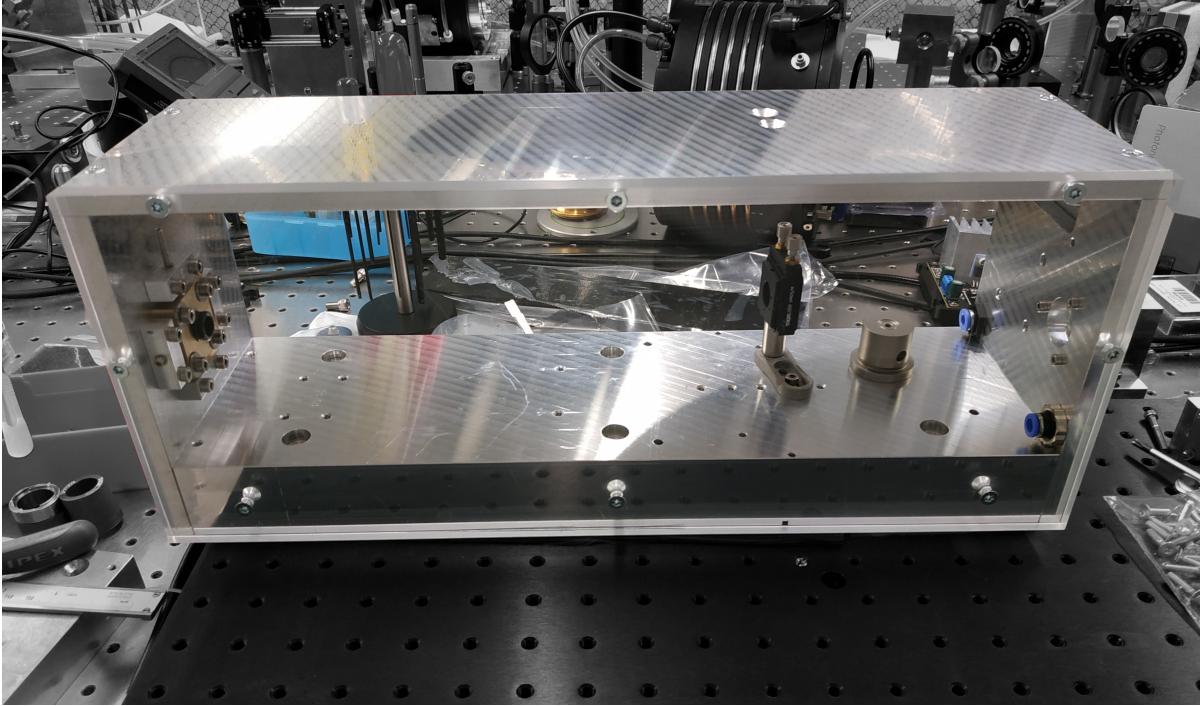
Figure 26: Closed container in which the laser is mounted.

4 Experiments

4.1 Efficiency

By applying different pump power and measuring the output power, the efficiency as defined in (4) was determined. The slope is expected to be linear with a lasing threshold.

Figure 27 shows the efficiency of the presented laser, where a slope efficiency of 58% was achieved. Apart from a single measurement, the linear fit lies within the error bound and therefore indicates no parasitical effects such as thermal lensing in this range of operation. Further, the lasing threshold was found at 6.28 W, which is the point of interception of the x-axis and the linear fit. An error of 10 mW was taken into account for the readings of the power meter. In this measurement the highest output power was measured to be 550 mW, limited by the power meter.

4.2 Tuning the Laser Frequency Using the Temperature of the BGTI

By applying a different current on the Peltier element, the temperature and thus the index of refraction of the BGTI can be changed. Subsequently, the optical path length of the cavity is changed, which
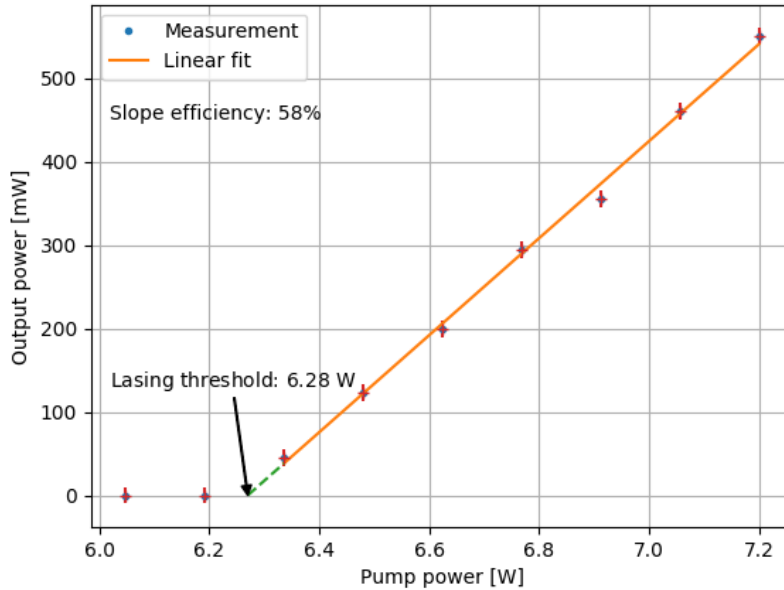
Figure 27: Determination of the efficiency of the thin-disk laser using a linear fit. The pump power was calculated from the input current applied on the diode laser which is used as pump light.

has an impact on the frequency of the laser. For a temperature change of 0.13 K and the values

$$L = 50 \text{ cm},$$
$$n_e = 1.5433 \quad \text{and}$$
$$\frac{\mathrm{d}n}{\mathrm{d}T} = -5.5 \cdot 10^{-6} \frac{1}{\text{K}},$$

the optical path length of the cavity changes by a factor of $-1.1 \cdot 10^{-6}$. For different temperatures, the frequency shift is analyzed using the reference cavity as described in Section 2.3.

Figure 28 shows the dependence of the frequency on the temperature, where some examples of raw data are shown in Figure 29. The laser output switches from single to double mode operation in the range of 20.900 °C to 21.075 °C. The uncertainty in temperature arises from the precision of the thermometer, whereas the error in the frequency arises from the measurement using the reference cavity. The decrease in frequency for higher temperatures than 21.050 °C requires further investigation. Comparing Figure 29 (c) to Figure 29 (d) shows that the total intensity of the laser remains constant in this measurement for changing temperature, which shows that a change in temperature does not lead to misalignment or thermal lensing effects within the scope of measurement accuracy. In conclusion, the temperature regulation can be used to modify the frequency of the laser, thereby allowing Hänsch-Couillaud locking in further developments of the laser.

4.3 Tuning the Laser Frequency Using the Piezo on the End Mirror

As mentioned in Section 3.1, the piezo can be used to change the length of the cavity and therefore allowing to adapt the frequency of the laser. In order to show the effect of the piezo on the frequency, different voltages were applied on the piezo and the frequency measured.

Figure 30 (a) shows the dependence of the laser frequency on the applied voltage on the piezo. A linear decrease in frequency is visible before switching to the next mode. However, the slope of the linear fits steepens for increasing voltage. Therefore, it is assumed that the piezo does not respond linearly on the applied voltage, which is a limitation to the stability of the laser, as the piezo is used
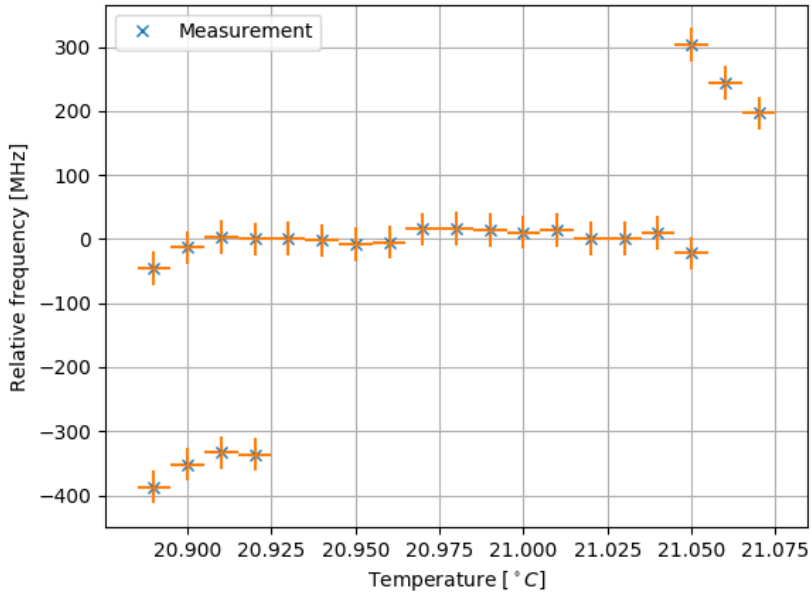
Figure 28: Measured frequency of the thin-disk laser for varying temperature of the BGTI. The y-axis is scaled so that the middle frequency was arbitrarily set to 0 and the average distance to the adjacent frequency equals 300 MHz, which corresponds to one *FSR* in this setup. Changing the temperature of the BGTI by 0.13 °C leads to a shift of one *FSR* in frequency of the laser.

for the Hänsch-Couillaud locking. However, for small frequency changes, the piezo approximately responds linearly. A further limitation is shown in Figure 30 (b), where the intensity of the beam with the corresponding frequency is plotted as a function of the voltage. In the range of high voltages i.e. from 110 V to 160 V the intensity is constant, whereas in the lower voltages, the intensity decreases. Assuming that the piezo does not perfectly expand in the direction of the optical axis, the decrease in intensity can be explained by a misalignment of the setup at low voltages. This limitation was not expected and will be tackled in a next step of improvement of the laser. Overall, the laser allows tuning in frequency by applying different voltages on the piezo, although large excursions lead to severe misalignment.

4.4 Locking the Laser Frequency Using the Hänsch-Couillaud Locking

If this laser should be used as a seed laser, an important requirement is that its frequency does not drift. This problem can be avoided using the Hänsch-Couillaud locking method, which will be quantitatively tested in the following measurement.

Figure 31 (a) and (b) shows the measured error signal (polarization difference signal as described in Section 2.5) over a time period of 50 s in free running mode. The linear drift visible in Figure 31 (a) as well as the discontinuity around 35 seconds in Figure 31 (b) indicating a mode-hop point out the importance of the Hänsch-Couillaud locking. When locked, frequency drifts are largely suppressed and the laser runs on a single mode for hours. Figure 31 (d) shows a typical trace of the error signal.

Using a discrete Fourier transformation, the measurements shown in Figure 31 (a) and (c) are compared in frequency space as shown in the mode plot of Figure 32. In the range of 10^{-2} Hz to 2 Hz the Hänsch-Couillaud locking leads to a significant suppression of noise. This is especially important and desired as slow drifts arise from low frequencies. For higher frequencies than 2 Hz the signals are exposed to the same amplitude of noise, where the lock does not lead to a substantial decrease in noise. In conclusion, the Hänsch-Couillaud locking works as expected by suppressing slow drifts in the laser frequency.
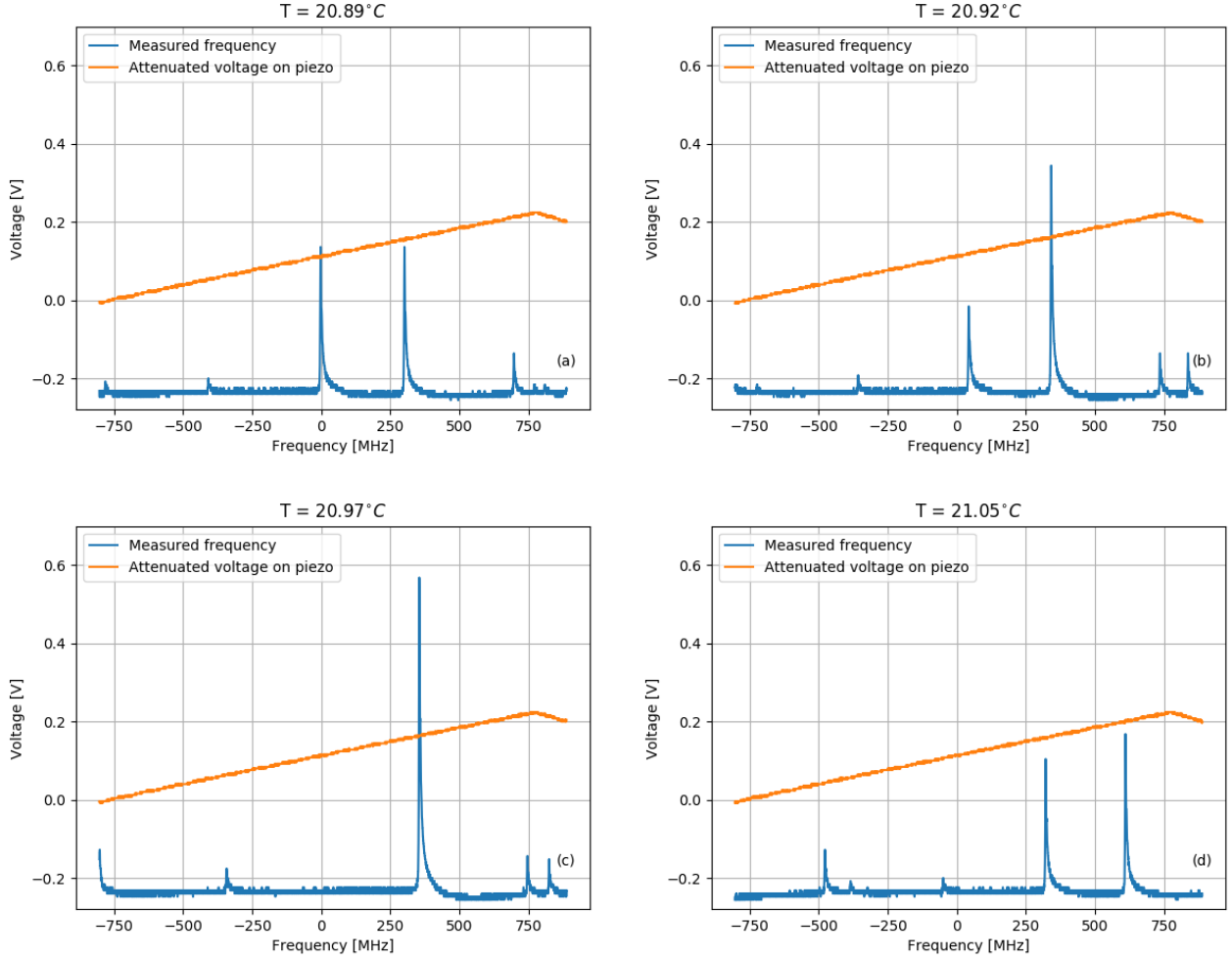
Figure 29: Spectrum of the PGTI laser at different temperatures. The spectra were recorded by scanning the reference cavity with a piezo. The signal to the piezo is attenuated by 100. Scaling was done by arbitrarily setting the first peak in (a) as reference and the average distance between two peaks to 300 MHz.

A further possibility to illustrate the effect of the Hänsch-Couillaud locking is by analyzing the excursion in polarization from the mean value in a histogram.

In Figure 33 the excursion from the mean value is shown in a normalized[4] histogram with corresponding gaussian fit. The binwidth was chosen using the Rice rule which is appropriate for approximately normally distributed data [20]. From the gaussian fit, the standard deviation can be determined which for the case of the measurement shown in Figure 31 (a) and (c) resulted in $\sigma_{NL} = 7.9$ mV and $\sigma_L = 6.7$ mV respectively. Therefore, the Hänsch-Couillaud locking leads to a slightly more narrow bandwidth. This was not specifically intended but is nonetheless of benefit. In summary, the measurements presented in Figure 31, 32 and 33 show that the Hänsch-Couillaud locking leads to an increased stability by preventing drifts in laser frequency.

---

[4]The area of the histogram is normalized to unit area.
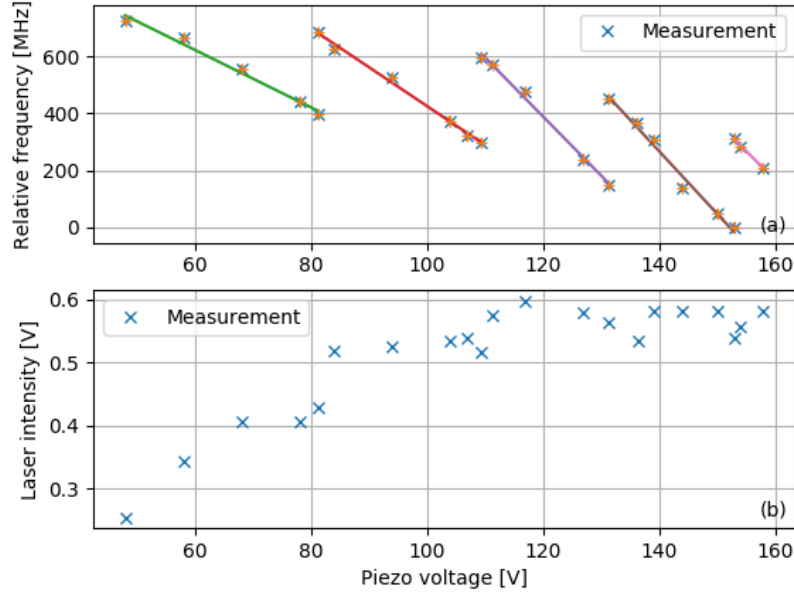
Figure 30: (a): Measured frequency of the thin-disk laser for different laser cavity lengths induced by the piezoelectric element attached behind the out coupling mirror. The green, red, violet, brown and pink curves are linear fits for a specific mode. (b): Corresponding to the frequency measurements, this plot shows the laser signal strength on the oscilloscope. At double mode operation, the intensities of the two peaks were added together. The significant decrease in amplitude for the initial measurements (< 80 V) might occur due to a misalignment of the laser arising from the piezoelectric element. Scaling of the frequency was done by setting the lowest frequency to zero and the mean distance between two modes to 300 MHz.
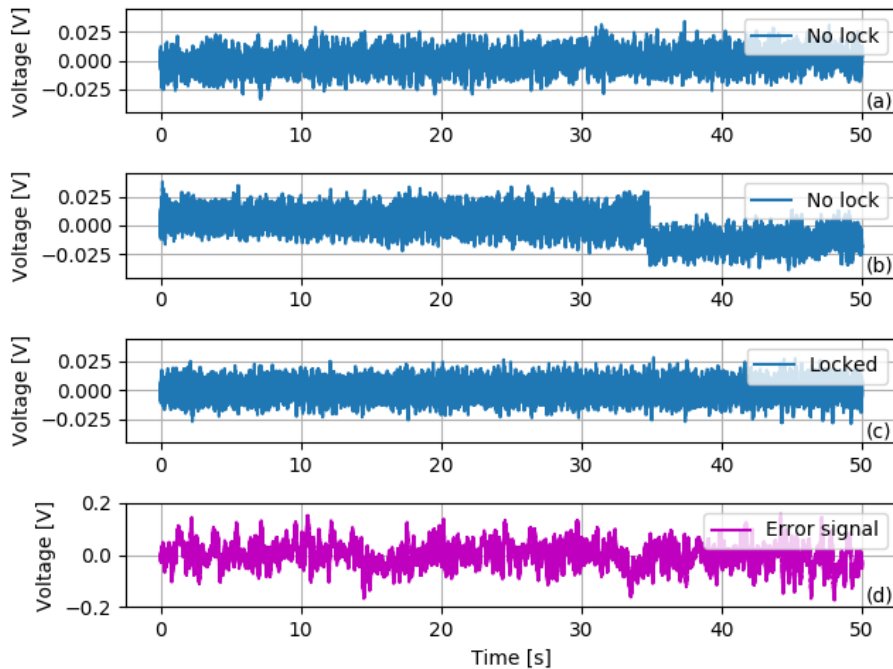
Figure 31: (a) and (b): Measured Hänsch-Couillaud error signal of the laser without locking. In (b) the signal shows a mode hop (i.e. a discontinuity in the polarization), which can be prevented by locking the signal. (c): Measured polarization difference of the laser with Hänsch-Couillaud locking. (d): The corresponding feedback signal for the locking of measurement shown in (c).
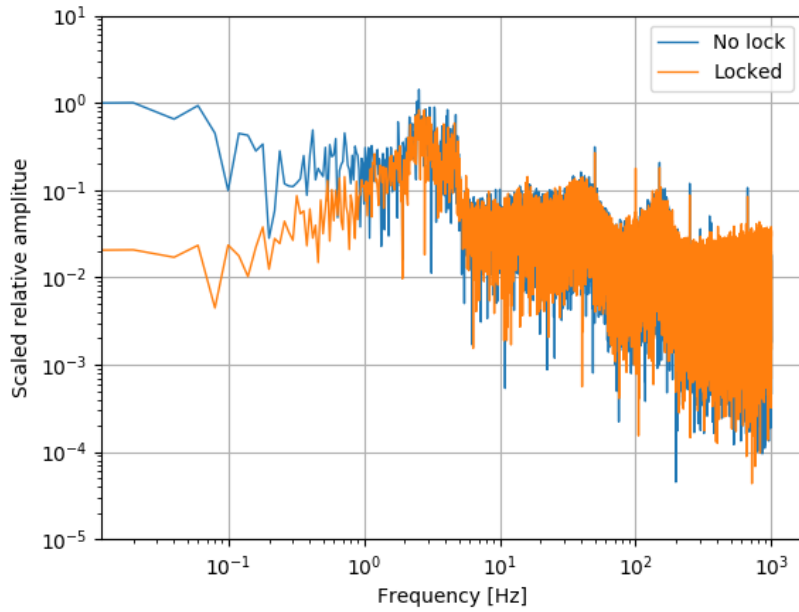
Figure 32: Fourier transformation of the signal shown in Figure 31 (a) and (c). Scaling was done by setting the lowest frequency of the free running signal to 1. It shows, that the Hänsch-Couillaud locking has an impact on the low frequency noise.
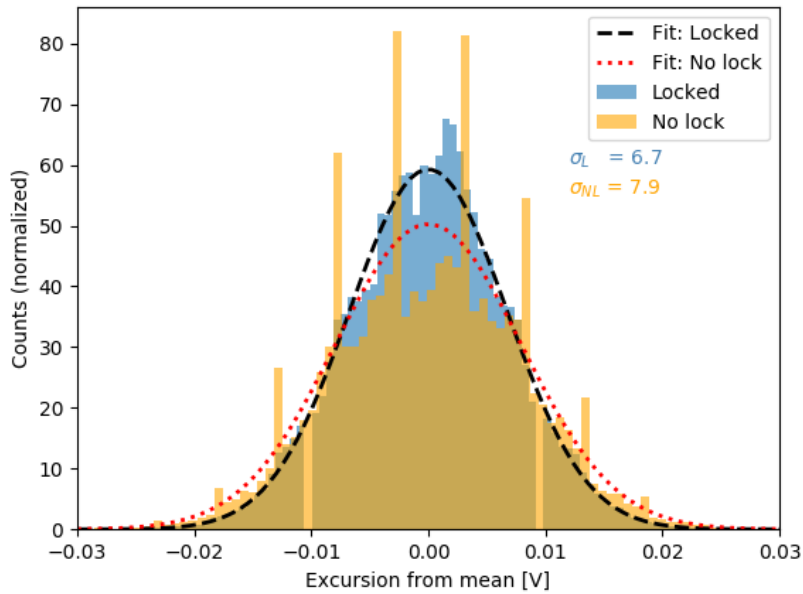
Figure 33: Histogram of the deviation from the mean of the error signal measurement shown in Figure 31 (a) and Figure 31 (c). The standard deviation is given in mV. The binwidth in both of the histograms were calculated using the Rice rule [20] and normalized to unit area. The smaller standard deviation of the fit for the locked signal shows, that the excursion from the mean over a period of 50 s is decreased and, therefore, the signal fluctuating in a smaller range than without locking. This is in accordance with Figure 32, which shows that the Hänsch-Couillaud locking compensates for low frequency noise.

5 Conclusion

Taking the requirements of the experiment to determine the Zemach radius of the proton into account, a thin-disk laser containing a polarizing Gires-Tournois interferometer was developed. To the best knowledge of the author, the presented laser is a first of its kind. Indeed, it was theoretically derived and experimentally shown that the polarizing Gires-Tournois interferometer functions as a frequency-selective element and is capable of enforcing single-frequency operation. The possibility of cooling the polarizing Gires-Tournois interferometer from the back side, makes it an ideal component for single-frequency operation in high power lasers. Furthermore, its suitability as frequency dependent polarizer for the Hänsch-Couillaud locking was illustrated. Beside of mechanical measures to minimize vibrations, the frequency of the laser is stabilized via a piezo using a Hänsch-Couillaud locking leading to a significant decrease in low frequency noise up to 2 Hz. This is, however, limited by the piezo which currently reveals nonlinear behaviour and additionally induces a misalignment of the setup. Even though the maximal measured output power was (550 ± 10) mW, the design of the presented laser allows power scaling to significantly higher powers. In a next step the temperature regulation of the birefringent Gires-Tournois interferometer can be included and thereby further increasing the frequency stability of the laser.

Acknowledgement

References

[1] Peter J Mohr et al. Codata recommended values of the fundamental physical constants: 2010. *J. Phys. Chem. Ref. Data*, 41(4):043109, 2012.

[2] Randolf Pohl et al. The size of the proton. *nature*, 466(7303):213–216, 2010.

[3] Aldo Antognini et al. Proton structure from the measurement of 2s-2p transition frequencies of muonic hydrogen. *Science*, 339(6118):417–420, 2013.

[4] Arne Thomsen. Small signal gain of a zero-phonon line pumped yb:yag thin disk. 2018.

[5] Aldo Antognini et al. Proposal for an experiment at psi - hyperfine splittings in muonic hydrogen and 3he. 2016.

[6] Clara Peset and Antonio Pineda. Model-independent determination of the two-photon exchange contribution to hyperfine splitting in muonic hydrogen. *Journal of High Energy Physics*, 2017(4):60, 2017.

[7] Ivo Schulthess. Improvement of the laser system for measuring the hyperfine splitting in muonic hydrogen. 2018.

[8] Karsten Schuhmann et al. Polarizing gires-tournois interferometer as intra-cavity frequency-selective element in high-power lasers. In *Components and Packaging for Laser Systems IV*, volume 10513, page 105131A. International Society for Optics and Photonics, 2018.

[9] Jakub Novak. *Diode pumped thin disk lasers for high repetition rate picosecond OPCPA pumping*. PhD thesis, 11 2016.

[10] Joerg Koerner et al. Measurement of temperature-dependent absorption and emission spectra of yb: Yag, yb: Luag, and yb: Caf 2 between 20 c and 200 c and predictions on their influence on laser performance. *JOSA B*, 29(9):2493–2502, 2012.

[11] Jeff Hecht. *Understanding lasers: an entry-level guide*. John Wiley & Sons, 2018.

[12] Adolf Giesen, H Hügel, A Voss, K Wittig, U Brauch, and H Opower. Scalable concept for diode-pumped high-power solid-state lasers. *Applied Physics B*, 58(5):365–372, 1994.

[13] Tracey Ryba, Sebastian Zaske, Sven-Silvius Schad, and Alexander Killi. Latest advances in high power and high brightness laser technology. In *Solid State Lasers XXVIII: Technology and Devices*, volume 10896, page 108960W. International Society for Optics and Photonics, 2019.

[14] GM Graf. Elektrodynamik. 2019.

[15] Steven Johnson. Quantum electronics. 2020.

[16] Kyle S Gardner, Richard H Abram, and Erling Riis. A birefringent etalon as single-mode selector in a laser cavity. *Optics express*, 12(11):2365–2370, 2004.

[17] TW Hänsch and B Couillaud. Laser frequency stabilization by polarization spectroscopy of a reflecting reference cavity. *Optics communications*, 35(3):441–444, 1980.

[18] Gianni Blatter. Theorie der wärme. 2011.

[19] Richard M. Martin. Piezoelectricity. *Phys. Rev. B*, 5:1607–1613, Feb 1972.

[20] David M Lane, David Scott, Mikki Hebl, Rudy Guerra, Dan Osherson, and Heidi Zimmer. *An Introduction to Statistics*. Rice University, 2017.